SUPPORTING INFORMATION

Monodisperse long-chain sulfobetaine-capped $CsPbBr_3$ nanocrystals and their superfluorescent assemblies

Franziska Krieg,[†,‡] Peter C. Sercel,[§,#] Max Burian,[‖] Hordii Andrusiv,[†,‡] Maryna I. Bodnarchuk,[†,‡] Thilo Stöferle,[¶] Rainer F. Mahrt,[¶] Denys Naumenko,[⊥] Heinz Amenitsch,[⊥] Gabriele Rainò,[†,‡] and Maksym V. Kovalenko[†,‡,*]

[†]Institute of Inorganic Chemistry, Department of Chemistry and Applied Biosciences, ETH Zürich, Vladimir Prelog Weg 1, CH-8093 Zürich, Switzerland

[‡]Laboratory for Thin Films and Photovoltaics, Empa – Swiss Federal Laboratories for Materials Science and Technology, Überlandstrasse 129, CH-8600 Dübendorf, Switzerland

[§] Center for Hybrid Organic Inorganic Semiconductors for Energy, 15013 Denver West Parkway, Golden, CO, 80401 USA

[#]Department of Applied Physics and Materials Science, California Institute of Technology, Pasadena, California 91125, USA

[‖]Swiss Light Source, Paul Scherrer Institut, 5232 Villigen PSI, Switzerland

[¶]IBM Research Europe - Zurich, Säumerstrasse 4, 8803 Rüschlikon, Switzerland

[⊥]Institute of Inorganic Chemistry, Graz University of Technology, Stremayrgasse 9/V, 8010 Graz, Austria

CHEMICALS

The following reagents were used as received: Cs_2CO_3 from Fluorochem, lead(II) acetate trihydrate (99.99%), bromine (99.9%), 1-octadecene (ODE, technical grade), 3-(N,N-dimethyloctadecylammonio)propanesulfonate (ASC18, >99%), ethylacetate (HPLC grade, ≥99.7%), mesitylene (98%) and oleic acid (90%, OA) from Sigma Aldrich/Merck, toluene (for synthesis) and acetone (HPLC grade) from Fischer and trioctylphosphine (>97%, TOP) and oleylamine (>95%, OLA) from STREM. For NC purification in the glove box ultra-dry solvents were used. Toluene was dried in a molecular-sieves-based solvent drying system to achieve water content <5 ppm and then stored in a nitrogen filled glove box over molecular sieves. Ultra dry polar solvents (acetone and ethylacetate) were delivered from Acros.

SYNTHESIS

Cs-oleate 0.4 M in ODE. Cs_2CO_3 (1.628 g, 5 mmol), OA (5 mL, 16 mmol) and ODE (20 mL) were evacuated upon heating to 120 °C until the completion of gas evolution.

Pb-oleate 0.5 M in ODE. Lead (II) acetate trihydrate (4.607g, 12 mmol), OA (7.6 mL, 24 mmol) and ODE (16.4 mL) were mixed in a three-necked flask and evacuated upon heating to 120 °C until the complete evaporation of acetic acid and water.

TOP-Br_2 0.5 M in toluene or mesitylene. TOP (6mL, 13 mmol) was mixed with toluene/mesitylene (18.7 mL) and bromine (0.6 mL, 11.5 mmol) under inert atmosphere.

Zwitterion-capped $CsPbBr_3$ NCs. A scaled-up version of our previously published procedure was adopted.[1] Pb-oleate (5 mL, 0.5M, 0.0025 mol), Cs-oleate (4 mL, 0.4M, 0.0016 mol), ASC18 (0.215 g, 0.5 mmol) and ODE (10 mL) were combined in a 50-mL three-necked-flask and heated to 120 °C under vacuum. Once the gas evolution stopped, the mixture was switched to argon and the temperature adjusted to 100-180 °C. After reaching the reaction temperature, TOP-Br_2 (5 mL, 0.5M, 0.0025 mol) was injected and the reaction was cooled immediately with an ice-bath. Larger NCs were grown at 180 °C using higher volume of ODE (50 mL, 100-mL flask). Different synthesis batches characterized in this work are labelled by numbers **1, 2, 3, …** (in appearance order), each differing by the synthesis temperature and/or the amount of ODE (Tables S1-S6, Figures S1-S6).

SIZE SELECTION

Isolation. In our experience, conducting isolation procedures in air, even when using pre-dried solvents, led to differences in the amounts of antisolvent needed for precipitation as well as to the difficulties in maintaining the integrity of smaller NCs. We anticipate that low-humidity ambient environment will also lead to good repeatability of the results.

After cooling the reaction mixture, the flask was transferred into a nitrogen-filled glove box in order to minimize the rather uncontrolled effects of ambient humidity. While doing so, the flask was first evacuated to reduce the pressure before loading the flask into the antechamber. This evacuation led to the substantial evaporation of toluene reducing the crude solution volume to *ca.* 19 mL (in the case of TOPBr_2/toluene). For the fractional precipitation procedure, ultra-dry solvents were used. The crude solution was centrifuged at 29500 g at 17 °C for 10 minutes separating the NCs into a supernatant (**s**) and a precipitate (**p**) fractions. Only for NCs grown at 150 °C and above, the **p** constitutes a substantial fraction. The supernatant (**s**) and, if applicable, the precipitate (**p**) were subsequently and separately subjected to size-selective precipitation, as described below. The first supernatant fraction and the last precipitate fraction contain the largest and the least colloidally stable NCs.

Size-selection using supernatant s. As shown in Figure 1 (Main Text) the fractional isolation of the supernatant proceeds through portion- wise anti-solvent addition (ethyl acetate or acetone, specified below for each synthesis batch in Tables S1-S6 and Figure S1-S6), followed by centrifugation (29500 g at 17 °C, 10 minutes). The supernatant continues in the purification cycle, until no luminescence of the supernatant is observed, while the precipitate of each cycle constitutes an isolated fraction of NCs (for instance, **1s**f1, **1s**f2, **1s**f3….). These fractions are redispersed in toluene (1-3 mL).

Besides containing largest NCs, the first fractions can also contain NCs that are less colloidally stable for reasons other than their weight (size). This can result in a deviation from the emission trend and is often also evidenced by lower QY values compared to the rest of the samples in the selection series. Apart from this effect, the QY remains high throughout the entire series.

Size-selection using precipitate p. The initial precipitate of the crude solution (**p**) can be size-fractioned by increasing the amount of toluene used to disperse the NCs in each cycle (see Figure 1) followed by centrifugation (29500 g at 17 °C for 10 minutes). Here the precipitate continues in the cycle, until it can no longer be dispersed, while the supernatants are collected as NC fractions and are labelled (for instance, **1p**f1, **1p**f2, **1p**f3…). So received fractions

can be used as is for measurements or purified further, by up to 3 more precipitation and redispersion cycles using acetone and toluene as a nonsolvent and solvent.

CHARACTERIZATION

Absorption spectra. All optical characterization was performed at ambient conditions. UV-Vis absorption spectra of colloidal NCs were collected using Jasco V670 and Jasco V770 spectrometers in transmission mode. The wavelength of the first and second excitonic transition was determined using the minima of the second derivative of the absorption spectra. The NC concentrations and hence the yields of each fraction were determined form absorption spectra using the method of Maes *et al*.[2]

Photoluminescence (PL). Fluorolog iHR 320 Horiba Jobin Yvon or Fluoromax 4 Horiba Jobin Yvon spectrofluorometers were used to acquire steady-state PL spectra from solutions, using excitation at 350-400 nm. FWHM values were obtained using a Gaussian model to fit the full spectrum. Absolute PL QYs of films and solutions were measured with Quantaurus-QY Absolute PL quantum yield spectrometer from Hamamatsu. Time-resolved PL traces were acquired in solution using a FluoTime300 spectrometer from PicoQuant. Samples were excited using a 355 nm, the detection was set at the PL peak maximum for each sample. Time resolved PL traces were fit to a single exponential decay model

$$y = y_0 + Ae^{-(x-x_0)/\tau} \quad (1)$$

with fixed x_0 values in agreement with the experimental delay times. The PL lifetimes τ are tabulated below (Tables S1-S6). A single exponential decay is in good agreement with the traces received for small NCs. Larger NCs have the tendency to become continuously more biexponential with increasing size. For consistency, the same single-exponential model was used throughout the analysis. Alternatively, the traces were fitted with a biexponential model of the same form. In this case the average lifetime was used to avoid bias due to over parametrization. The results received from either model agree well (see Table S8).

Electron microscopy. TEM images were collected using Hitachi HT7700 microscope operated at 100 kV and a JEOL JEM-2200FS microscope operated at 200 kV. HAADF-STEM images were collected at cryo-conditions (holder cooled with liquid nitrogen) on a Tecnai F30 (Thermo Fisher Scientific) operated at 300 kV with a point resolution of *ca*. 2 Å. Scanning electron microscopy (SEM) of the $CsPbBr_3$ super crystals on silicon substrates were performed with secondary electrons (SE) on a 1530 Gemini (Zeiss; field emission gun (FEG)) using a low voltage electron beam (Vacc = 1 KV) to minimize charging. EM images were processed using Fiji.[3]

Table S1. Size selection of ASC18-capped $CsPbBr_3$ NCs (grown at 100 °C using $TOPBr_2$ in toluene, *ca*. 19 mL of crude solution) using **acetone** as anti-solvent.

fraction	acetone (mL)	solvent: antisolvent ratio	emission wavelength (nm)	FWHM (nm)	FWHM (meV)	1st excitonic maximum (nm)	2nd excitonic maximum (nm)	PL lifetime (ns)	PL QY (%)	yield (mg)
1sf1	18	1.1	499	25.3	126.1	482	463	5.2	29	16.6
1sf2	20	1.0	502	19.8	97.6	491	478	5.9	73	143.2
1sf3	22	0.9	498	20.0	99.9	487	-	5.5	75	128.7
1sf4	24	0.8	496	20.4	103.2	481	-	6.8	73	148.9
1sf5	26	0.7	488	22.1	115.1	472	-	5.2	71	66.3
1sf6	30	0.6	481	22.8	122.3	466	-	5.2	69	22.9
1sf7	34	0.6	479	22.2	119.9	462	419	5.2	62	17.3

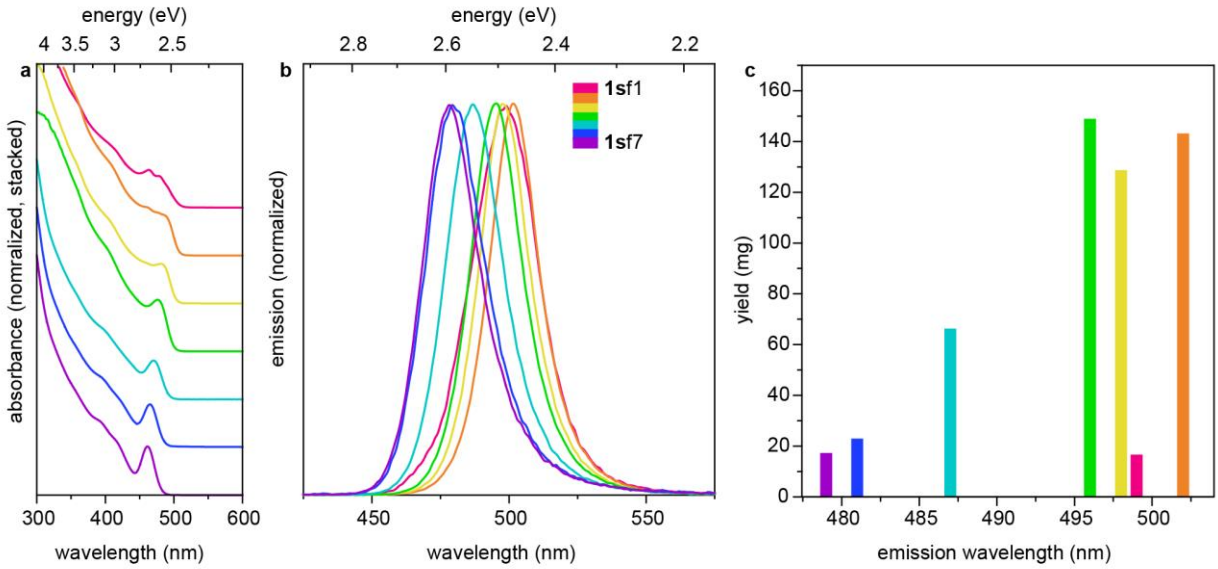

Figure S1. (a) Absorption and (b) normalized PL spectra of all fractions received from a crude solution of NCs grown at **100 °C** (acetone as antisolvent). The first fraction exhibits broader distribution of species. This can be explained considering that size-selective precipitation selects NCs based on their solubility, removing not only largest NCs, but also agglomerated ones, surface-damaged NCs *etc*. (c) Estimated yields of each fraction (in mg).

Table S2. Size selection of ASC18-capped NCs (grown at 130 °C using $TOPBr_2$ in toluene, *ca*. 19 mL of crude solution) using **ethyl acetate** as anti-solvent.

fraction	ethyl acetate (mL)	solvent to anti-solvent ratio	emission wavelength (nm)	FWHM (nm)	FWHM (meV)	1st excitonic maximum (nm)	2nd excitonic maximum (nm)	PL lifetime (ns)	PL QY (%)	average size (nm)	size standard deviation (nm)	yield (mg)
2sf1	20	1.0	514	16.9	79.4	509	496	7.6	56			25.8
2sf2	26	0.7	512	16.5	78.2	507	495	6.1	69	8.8	0.9	27.9
2sf3	32	0.6	511	16.5	78.3	505	492	5.6	69	8.6	1.0	40.9
2sf4	36	0.5	509	16.7	79.9	503	489	5.4	75	8.1	1.0	54.6
2sf5	40	0.5	507	16.9	81.7	501	483	4.9	68	7.5	0.7	42.5
2sf6	44	0.4	505	17.5	84.9	498	480	4.7	70	7.1	0.9	47.6
2sf7	54	0.4	505	18.0	87.5	495	475		66			114.0

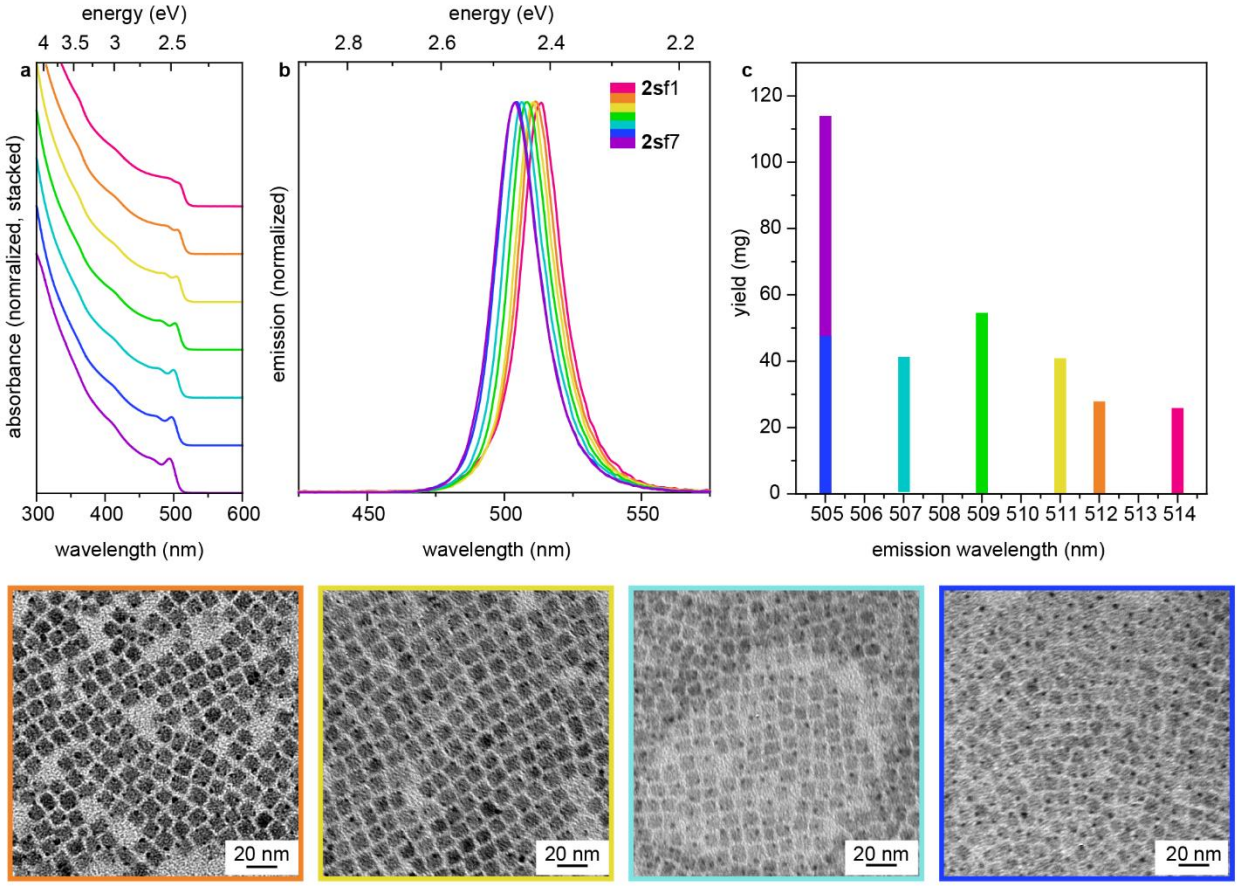

Figure S2. (a) Absorption and (b) normalized PL spectra of all fractions received from a crude solution of NCs grown at **130 °C** (ethyl acetate as antisolvent). (c) Estimated yields of each fraction (in mg).

Table S3. Size selection of ASC18-capped NCs (grown at 150 °C using$TOPBr_2$ in mesitylene, *ca*. 24 mL of crude solution) using **ethyl acetate** as anti-solvent.

fraction	ethylacetate (mL)	solvent to antisolvent ratio	emission wavelength (nm)	FWHM (nm)	FWHM (meV)	1st excitonic maximum (nm)	2nd excitonic maximum (nm)	PL QY (%)	average size (nm)	size standard deviation (nm)	yield (mg)
3sf1	14	1.71	511	19	90.3	508	489	79	5.4	0.9	41.9
3sf2	32	0.75	508	18	86.5	504	486	73	7.1	1.3	30.4
3sf3	38	0.63	507	18	86.9	502	483	57	7.3	1.2	29.0
3sf4	42	0.57	504	18	87.9	500	480	72	6.7	1.1	20.6
3sf5	44	0.55	502	18	88.6	497	478	65	6.3	0.9	13.1
3sf6	48	0.50	502	19	93.5	497	476	70	6.4	0.7	23.9
3sf7	54	0.44	501	19	93.9	495	472	65	5.8	0.9	52.6
3sf8	60	0.40	499	20	99.6	492	468	48	4.7	0.7	49.9
3sf9	66	0.36	496	21	105.9	488	460	77	5.1	0.8	63.0

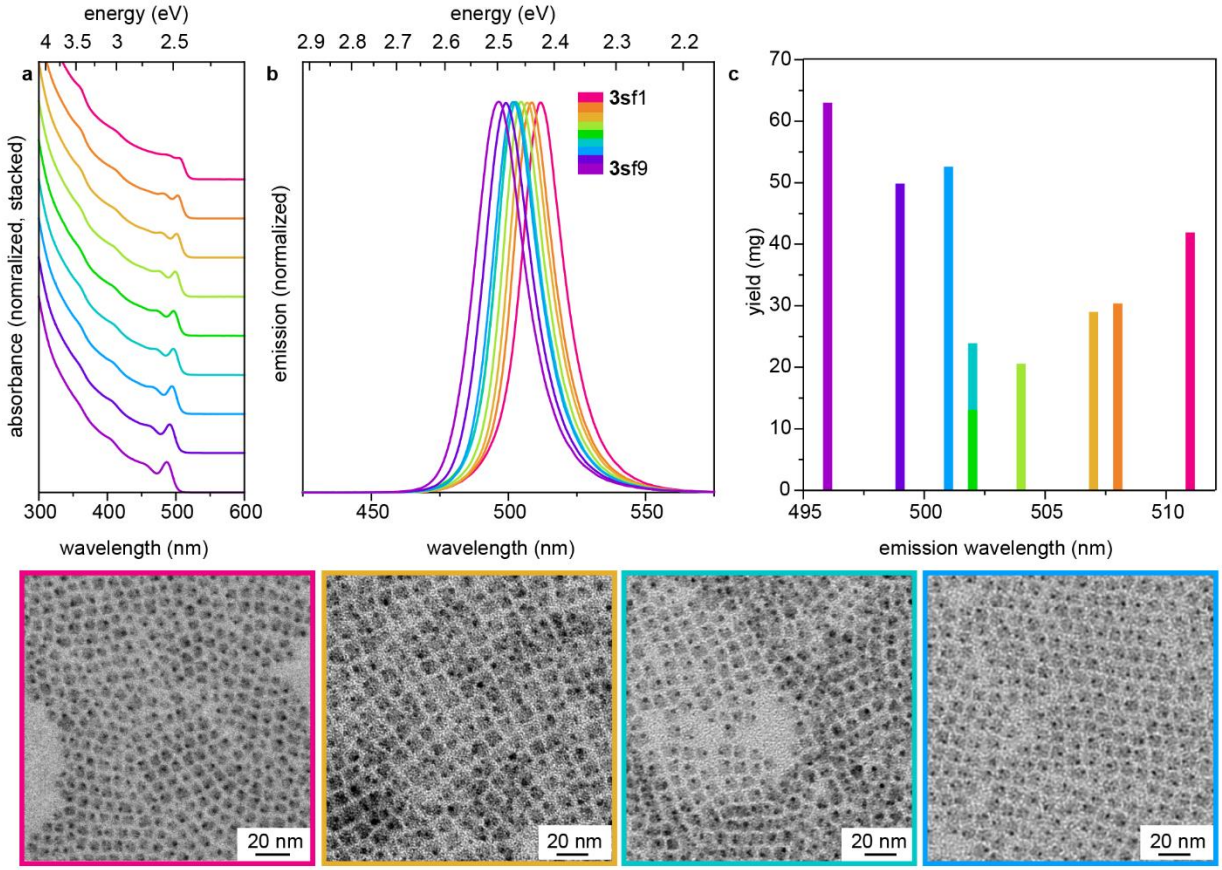

Figure S3. (a) Absorption and (b) normalized PL spectra of all fractions received from a crude solution of NCs grown at **150 °C** (ethyl acetate as antisolvent). (c) Estimated yields of each fraction (in mg). The same data set is presented in Figure 1 of the Main Text.

Table S4. Size selection of ASC18-capped NCs (grown at 150 °C using$TOPBr_2$ in mesitylene, *ca*. 24 mL of crude solution) using **acetone** as anti-solvent.

fraction	acetone (mL)	solvent to antisolvent ratio	emission wavelength (nm)	FWHM (nm)	FWHM (meV)	1st excitonic maximum (nm)	2nd excitonic maximum (nm)	PL lifetime (ns)	PL QY (%)	average size (nm)	size standard deviation (nm)	yield (mg)
4sf1	26	0.92	497	27.4	137.5	484	-	-	83	-	-	10.3
4sf2	32	0.75	508	21.4	103.1	504	484	6.5	84	7.8	0.91	3.2
4sf3	34	0.71	506	20.4	98.9	501	481	-	87	6.4	0.9	15.7
4sf4	36	0.67	504	20.6	100.5	497	475	-	87	6.8	0.99	29.9
4sf5	38	0.63	503	20.5	100.6	492	466	-	86	-	-	64.4
4sf6	40	0.60	501	20.2	99.9	488	455	5.9	83			100.4
4sf7	42	0.57	495	20.95	106.0	483	450	4.6	84			29.3
4sf8	44	0.55	490	22.2	114.6	480	445	-	83	3.9	0.64	16.4
4sf9	48	0.50	488	23.2	121.0	478	439	-	83	-	-	14.1

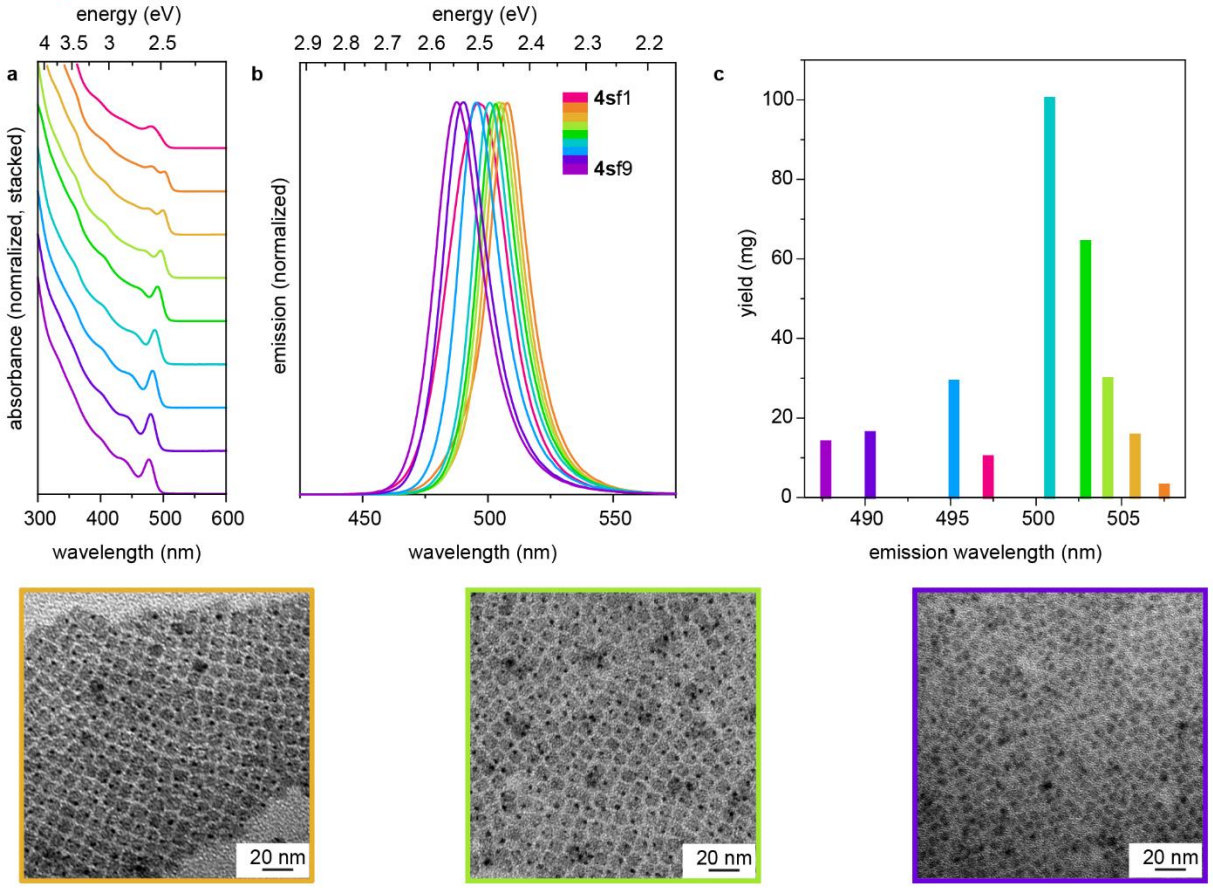

Figure S4. (a) Absorption and (b) normalized PL spectra of all fractions received from a crude solution of NCs grown at **150 °C** (acetone as antisolvent). The first fraction exhibits broader distribution of species. This can be explained considering that size-selective precipitation selects NCs based on their solubility, removing not only largest NCs, but also agglomerated ones, surface-damaged NCs *etc*. (c) Estimated yields of each fraction (in mg).

Table S5. Size selection of ASC18-capped NCs (grown at 180 °C using $TOPBr_2$ in toluene, *ca*. 11 mL of crude solution), using **ethyl acetate** as anti-solvent.

fraction	ethyl acetate (mL)	solvent to antisolvent ratio	emission wavelength (nm)	FWHM (nm)	FWHM (meV)	1st excitonic maximum (nm)	2nd excitonic maximum (nm)	PL lifetime (ns)	PL QY (%)	average size (nm)	size standard deviation (nm)	yield (mg)
5pf1	-	-	517	15.7	72.8	509	-	16.4	27	12	2	3.7
5sf1	5	2.2	517	15.8	73.5	510	-	17.3	12	14.2	1.8	2.8
5sf2	8	1.4	517	16.2	74.6	509	-	19.0	40	13.2	1.7	14.3
5sf3	12	0.9	516	16.0	74.1	508	-	15.1	58	11.7	1.6	14.0
5sf4	16	0.7	515	15.9	73.9	512	502	11.1	72	-	-	11.4
5sf5	21	0.5	514	15.7	73.4	511	500	8.3	35	9.7	1.2	6.9
5sf6	31	0.4	512	15.4	72.2	509	493	5.7	71	8.6	1.2	2.7

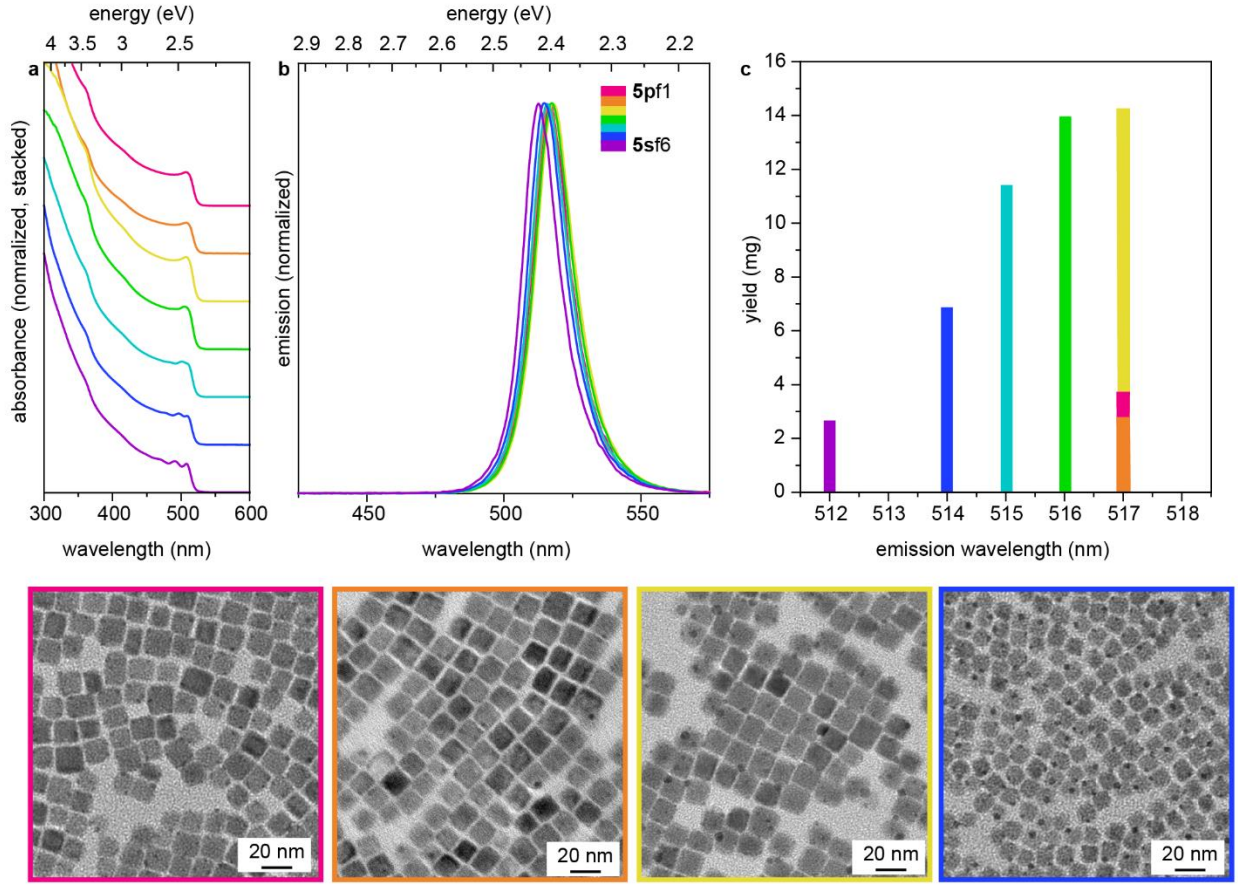

Figure S5. (a) Absorption and (b) normalized PL spectra of all fractions received from a crude solution of NCs grown at **180 °C** (ethyl acetate as antisolvent). (c) Estimated yields of each fraction (in mg).

Table S6. Size selection of ASC18-capped NCs (grown at 180 °C using $TOPBr_2$ in mesitylene, *ca*. 6 mL of crude solution), precipitate was selected by increasing the amount of toluene in redispersion.

fraction	toluene (mL)	Emission wavelength (nm)	FWHM (nm)	FWHM (meV)	1st excitonic maximum (nm)	2nd excitonic maximum (nm)	PL lifetime (ns)	PL QY (%)	average size (nm)	size standard deviation (nm)	yield (mg)
6pf1	1	514	16.7	78.4	511	-	9.86	76	11.3	1.3	1.50
6pf2	2	515	15.99	74.9	513	-	-	72	10.4	1.2	0.23
6pf3	3	516	16.2	75.5	514	-	13.25	53	13.0	1.3	0.85
6pf4	4	516	15.99	74.4	514	-	16.26	27	16.6	2.0	0.52
6pf5	5	516	15.87	73.8	514	-	-	33	15.7	2.0	0.02
6pf6	6	517	15.93	73.9	516	-	-	18	12.6	2.6	0.03

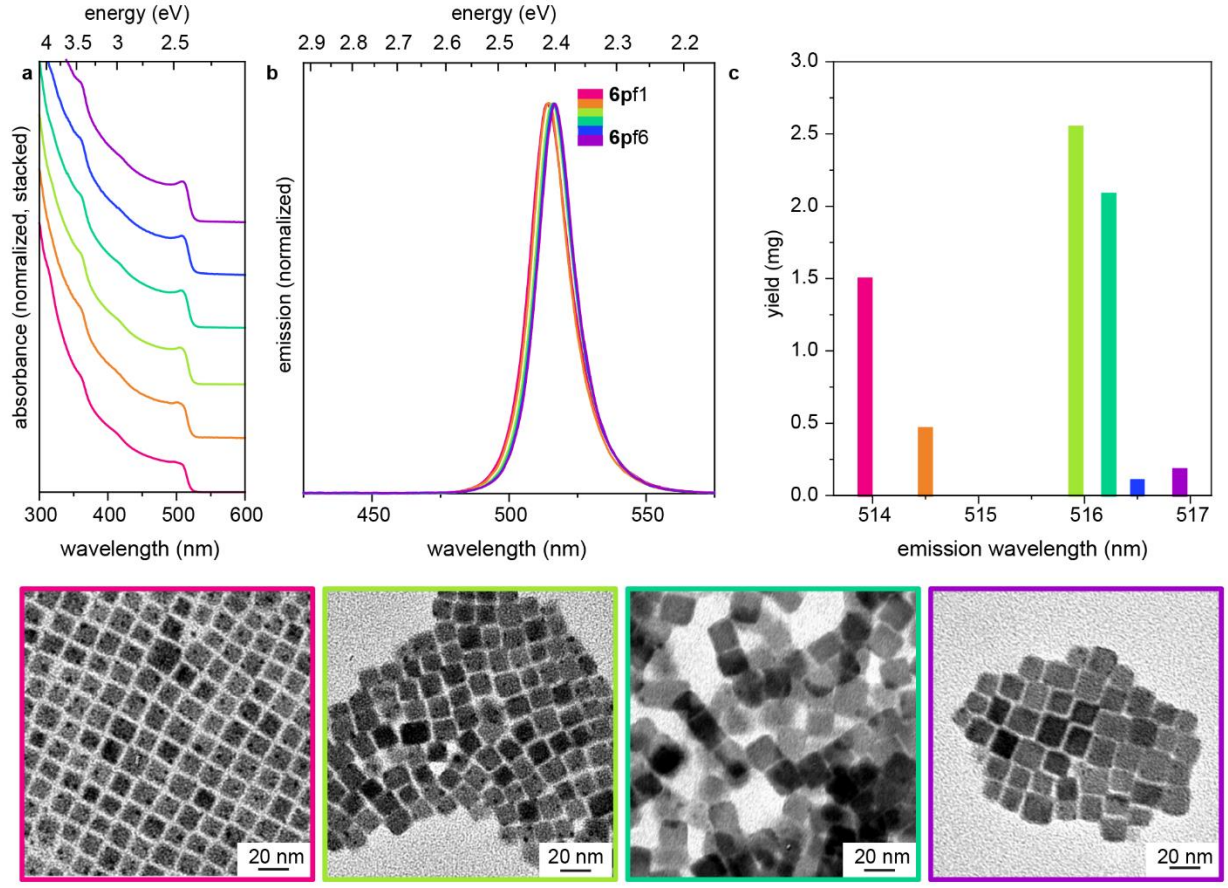

Figure S6. (a) Absorption and (b) normalized PL spectra of all fractions received from a crude solution of NCs grown at **180 °C** (precipitate fraction was size selected no anti solvent was used). The first fraction exhibits broader distribution of species. This can be explained considering that size-selective precipitation selects NCs based on their solubility, removing not only largest NCs, but also agglomerated ones, surface-damaged NCs *etc*. (c) Estimated yields of each fraction (in mg).

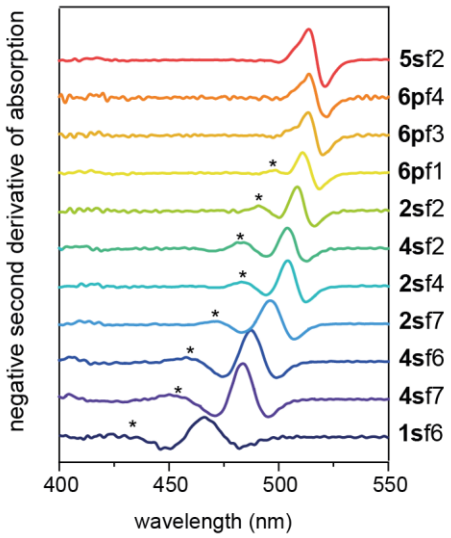

Figure S7. Negative second derivatives of the absorbance spectra shown in Figure 3a. The minima in the second derivative, *i.e*. the maxima in this representation, correspond to peak maxima in the 0th order curve. The stars denote the position of the 2nd excitonic transition as indicated in Figure 3a as well in the original spectra. It is clear from the symmetry of the 2nd derivative curves where the 2nd excitonic transition cannot be resolved, that there the 1st and 2nd excitonic peaks are convoluted based on the line shape.

SMALL-ANGLE X-RAY SCATTERING

Small-angle X-ray scattering (SAXS) measurements were performed at the Austrian SAXS beamline of the electron storage ring ELETTRA using a photon energy of 8 keV.[4] The beamline setup was adjusted to a sample to detector distance of 780 mm to result in an accessible q-range 0.12–9.5 nm^{-1}. All images were recorded using the Pilatus[3] 1M detector (Dectris, Switzerland) with 15 exposures of 5 seconds per sample to check for radiation damage. Reference patterns to calibrate the q-scale were collected of silver-behenate (*d*-spacings of 5.838 nm). All measurements were done using a 1.5 mm quartz flow cell capillary. The radial averaging and the image calibration were conducted using the SAXSDOG software.[5] All presented data was corrected for fluctuations of the primary intensity and the corresponding background (toluene) has been subtracted from each scattering pattern after transmission correction.

SAXS model fitting. Scattering patterns were fitted using an analytical model where the model intensity $I_{mod}(q)$ of the analytical model corresponds to polydisperse (Gaussian volume-distribution), orthorhombic parallelepipeds and is written as

$$I_{mod}(q) = BG + I_0 \cdot S_{SHS}(q) \cdot \sum_{i}^{N_{SD}} G(r_i, c, \sigma) \cdot V(r_i) \cdot F\left(q, r_i, \frac{b}{c}, \frac{a}{c}\right) \quad (2)$$

where BG denotes a constant background, $S_{SHS}(q)$ denotes the structure factor describing possible NC interaction and I_0 denotes the forward scattering intensity scalar. The fitting parameters are: (c) the first (smallest) NC side length, ($\frac{b}{c}$) the aspect ratio of the second to first NC side length, ($\frac{a}{c}$) the aspect ratio of the third to first NC side length and (σ) the standard-deviation of the size-distribution (relative).[6] The summation part of the equation represents the numerical average over the Gaussian distribution $G(r_i, a, \sigma)$, here consisting of N_{SD} = 51 discrete points. The size distribution is calculated over the range $a(1-3\sigma) < r_i < a(1+3\sigma)$ and is weighted by volume $V(r_i) = r_i^3 \cdot \frac{b}{c} \cdot \frac{a}{c}$. We calculate the formfactor contribution $F\left(q, r_i, \frac{b}{c}, \frac{a}{c}\right)$ describing the orthorhombic NC shape according to literature[7] such that $F(q=0) = 1$, where r_i denotes the shortest NC side length corresponding to the respective size-distribution weight such that the other sides are scaled by $\frac{b}{c}$ and $\frac{a}{c}$. Fitting results can be found in Table S7 – the model patterns are shown in Figure 2 and S8.

Scattering patterns were fitted in the angular regime of $0.13 < q < 4$ nm^{-1}, which shows characteristic form-factor scattering features of nanoparticles. The model intensity (see equation 2) was fitted by optimizing all parameters but keeping the background (BG) fixed. For all samples, we find outstanding agreement of experimental and model scattering patterns, as quantitatively evidenced by the goodnesss-of-fit value $\chi^2 < 1.11$ for all datasets.
For selected datasets, the full scattering pattern can only be fitted when including a sticky-hard-sphere structure factor contribution $S_{SHS}(q)$ describing nanocrystal interaction ($S_{SHS}(q) = 1$ for no interaction). A detailed model description can be found in literature.[8] In short, the model assumes a square-well potential, where the interaction force is defined by the potential well depth ε [ε > 0 for attractive and ε < 0 for repulsive interaction] and the potential well size $\lambda \cdot r_H$, where r_H denotes the hard-sphere radius [to reduce fitting uncertainties due to co-dependency of fitting parameters, we kept λ constant at 1.5 for all fits]. To obtain a comprehensible quantity from these parameters, we calculate the mean NC-NC (center to center) interaction distance according to $2 \cdot \lambda \cdot r_H$.

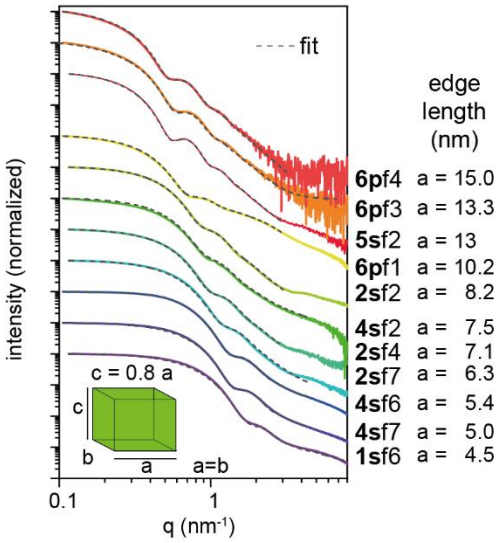

Figure S8. Small-angle X-ray scattering traces for the samples shown in Figure 3. The traces of samples **5s**f2 and **1s**f6 are also displayed in Figure 2 of the main text. Dashed lines show the fits to an orthorhombic model invariably resulting in cuboidal shape with one edge 20% shorter with respect to the two others. This direction is regardless of actual crystal structure direction and in agreement with crystallographic conventions named c. An overview over all fitting results, parameters and goodness of fit values are given in Table S7.

Table S7. Optimized fitting parameters of the SAXS full pattern refinement. For an explanation of the variables, see eq. 2 and the description above. Grey cells denote parameters that have been set as fixed during the fitting process. The "Avg. Error" denotes the mean uncertainty (std. dev.) of the retrieved model parameters over all datasets.

	BG	I_0	c Number distribution	c Volume distribution	b/c	a/c	σ	$2 \cdot \lambda \cdot r_H$	ϵ	χ^2
	[.]	[.]	[nm]	[nm]	[1]	[1]	[%]	[nm]	[.]	[.]
6pf4	0.048	37.05	11.69	12.05	1.14	1.28	9.9	-		0.77
5sf2	0.041	49.30	11.35	11.65	1.16	1.17	9.8	-		1.09
6pf3	0.067	14.78	10.62	11.02	1.19	1.25	10.6	-		1.82
6pf1	0.082	25.55	8.55	8.99	1.19	1.21	13.8	13.1	0.54	1.68
2sf2	0.042	31.23	6.92	7.53	1.18	1.18	17.6	11.0	1.64	0.96
4sf2	0.033	28.01	6.31	7.05	1.14	1.19	20.6	10.8	1.81	1.43
2sf4	0.039	20.13	6.05	6.51	1.17	1.19	16.2	10.7	1.48	0.91
2sf5	0.044	17.65	5.51	5.97	1.18	1.24	16.6	9.9	0.72	1.02
2sf7	0.043	15.76	5.09	5.48	1.24	1.22	16.3	-		1.41
4sf6	0.082	16.19	4.51	4.94	1.19	1.21	14.1	8.9	3.62	1.06
4sf7	0.090	12.24	4.23	4.58	1.19	1.22	12.8	-		1.23
1sf4	0.036	9.51	3.97	4.45	1.23	1.25	20.8	-		0.97
1sf6	0.042	9.00	3.62	3.79	1.25	1.26	12.1	-		1.05
Avg. error of single measurements [%]	-	1.98	3.23	3.23	9.56	8.93	14.3	27.3	44.9	

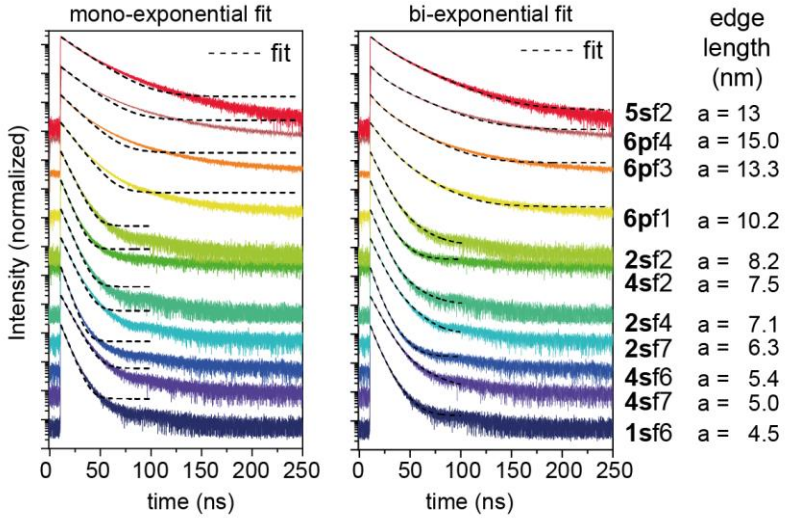

Figure S9. Time-resolved PL traces under 355 nm excitation for the samples shown in Figure 3, along with single-exponential and bi-exponential fits (dashed lines). Samples **5s**f2 and **1s**f6 are also displayed as inset in Figure 3d of the main text. The single-exponential fit agrees well with the data for at least two out of 4 measured orders of magnitude in intensity. Bi-exponential fitting was not used to keep the number of variables small and comparable. Average lifetimes obtained by the biexponential fitting agree well with the lifetimes received by mono-exponential fitting as can be seen from their comparison in Table S8.

Table S8. Fitting results for all time resolved PL traces measured. Including mono and biexponential models. The average lifetime in the biexponential model was calculated as $\tau_{average} = \frac{\tau_1 A_1 + \tau_2 A_2}{A_1 + A_2}$. The average lifetime is almost identical to the lifetimes received from the mono-exponential fit in particular for the points used in the lifetime fit (shaded gray). Except for few samples, the PL QYs are in the 60-70% range (±5% which is the instrument accuracy).

	mono-exponential			bi-exponential				
	emission (nm)	liftime (ns)	QY (%)	A_1 (au)	τ_1 (ns)	A_2 (au)	τ_2 (ns)	$\tau_{average}$ (ns)
1sf1	499	5.2	29	8523	4.36	1329	11.55	5.3
1sf2	502	5.9	73	9114	5.73	226	23.6	6.2
1sf3	498	5.5	75	9015	5.08	555	13.74	5.6
1sf4	496	6.8	73	8380	6.38	475	16.58	6.9
1sf5	488	5.2	71	8149	4.43	1507	9.6	5.2
1sf6	481	5.2	69	7974	4.48	1472	9.4	5.2
1sf7	479	5.2	62	7589	4.41	1801	8.92	5.3
2sf1	514	7.6	56	8081	6.53	1394	14.8	7.7
2sf2	512	6.1	69	8582	5.96	573	14.04	6.5
2sf3	511	5.6	69	8299	4.95	1362	10.04	5.7
2sf4	509	5.4	75	9159	5.14	374	14.06	5.5
2sf5	507	4.9	68	9836	4.77	235	15.4	5.0
2sf6	505	4.7	70	9844	4.56	203	15.56	4.8
5pf1	517	16.4	27	6293	9.49	3817	27.46	16.3
5sf1	517	17.3	12	2637	9.9	1490	30.5	17.3
5sf2	517	19	40	2195	10.98	1729	28.69	18.8
5sf3	516	15.1	58	2366	10.54	1332	23.3	15.1
5sf4	515	11.1	72	3102	8.316	1246	17.91	11.1
5sf5	514	8.3	35	4918	7.73	272	23.01	8.5
5sf6	512	5.7	71	3387	4.47	1268	8.95	5.7
4sf2	508	6.5	84	4784	6.5	4112	6.5	6.5
4sf6	501	5.9	83	18119	5.29	2377	11.8	6.0
4sf7	495	4.6	84	18471	4.07	2085	9.6	4.6
6pf1	514	9.86	76	18523	8.09	3249	20.8	10.0
6pf3	516	13.25	53	12906	7.088	8229	22.2	13.0
6pf4	516	16.26	27	5948	7.67	4349	26.88	15.8

THEORY

Quantum confinement model for excitons in NCs. Our purpose is to formulate expressions for the energies of excitons in non-cubic LHP NCs. We first note that conduction and valence bands in LHP NCs are each two-fold degenerate, each characterized by angular momentum J=1/2.[9] This being the case, a description of the confined excitons can be formulated in terms of a simple band effective mass model description, in contrast to the situation in semiconductors such as CdSe where valence band degeneracy requires a multi-band effective mass description. The problem boils down to solving the effective mass equation for an exciton within the NC:

$$\widehat{H}^{eff} f(\boldsymbol{r}_e, \boldsymbol{r}_h) = E_x f(\boldsymbol{r}_e, \boldsymbol{r}_h). \quad (3)$$

Here, $f(\boldsymbol{r}_e, \boldsymbol{r}_h)$ is the envelope function for the exciton, which is written as a function of the electron and hole coordinates, $\mathbf{r}_e$, $\mathbf{r}_h$, respectively, E is the exciton energy relative to the band gap, and the effective mass Hamiltonian for the electron/hole pair is given by the sum of their kinetic energies and their potential energy of interaction,

$$\widehat{H}^{eff} = -\frac{\hbar^2}{2m_h}\nabla_e^2 - \frac{\hbar^2}{2m_e}\nabla_h^2 - \frac{e^2}{\epsilon_{eff}|\boldsymbol{r}_e - \boldsymbol{r}_h|} \quad (4)$$

where ϵ_{eff} is the effective dielectric constant screening the electron/hole Coulomb interaction. This equation must be solved subject to the condition that the envelope function vanish on the NC surface. In NCs smaller than the exciton Bohr radius, a_x, it is a reasonable approximation to solve this equation by first neglecting the electron/hole Coulomb interaction, and then calculating the Coulomb correction in first order perturbation theory,[10] an approach which is known as the strong confinement approximation. Since the exciton radius in LHPs such as $CsPbBr_3$ is $a_x \sim 3$ nm, this approach is not valid in NCs that have been grown to date, which are universally larger than the exciton radius.

Intermediate confinement model for the lowest energy exciton states in cube-shaped NC. A variational approach to this problem of intermediate confinement in a cube shaped NC was described for the lowest energy exciton state in Becker *et al*.,[9] within the parabolic band approximation. That is, in Eq. 3 above, the effective masses were taken to be energy independent constants. Then the exciton energy was evaluated assuming an ansatz function for the exciton wavefunction as follows. First, writing the wavefunction of the ground electron and hole quantum confined levels in a nano-cube of edge length L, as,

$$\psi_S(x,y,z) = \sqrt{\frac{8}{L^3}}\cos\left(\frac{\pi x}{L}\right)\cos\left(\frac{\pi y}{L}\right)\cos\left(\frac{\pi\, z}{L}\right) \quad (5)$$

The wavefunction of the lowest, "S-S" exciton is assumed to be of the form,

$$f_{S-S}(\boldsymbol{r}_e,\boldsymbol{r}_h) = \frac{1}{\sqrt{N(\beta_{SS})}}e^{-\beta_{SS}|\boldsymbol{r}_e-\boldsymbol{r}_h|}\psi_S(\boldsymbol{r}_e)\psi_S(\boldsymbol{r}_h) \quad (6)$$

where the term involving the correlation parameter β brings in correlation in the motion of the electron and hole. Using this ansatz function, the exciton energy E_x is calculated as,

$$E_x = \frac{\langle f|\widehat{H}^{eff}|f\rangle}{\langle f|f\rangle} \quad (7)$$

The optimum variational parameter $\beta_{opt} = \beta_{opt}(L)$ is determined as the value of β which minimizes the energy for a NC of a given edge length, L. For large sizes it has been shown that $\beta \to 1/a_x$ where a_x is the bulk exciton Bohr radius.[11]

This approach can be extended to describe higher energy exciton levels. For example, the cartoon level structure in Figure S10 shows the two lowest energy optically allowed exciton transitions in a cube shaped NC. In addition to the ground S-S exciton, in a cube-shaped NC there are 3 degenerate P-P exciton transitions. For these excitons, the carrier wavefunctions can be written in the form,

$$\psi_P(x,y,z) = \sqrt{\frac{8}{L^3}}\cos\left(\frac{\pi x}{L}\right)\cos\left(\frac{\pi y}{L}\right)\mathrm{Sin}\left(\frac{2\,\pi\, z}{L}\right) \quad (8)$$

where the wavefunction has been written explicitly for the P_z state; and the exciton wavefunction is written using the ansatz,

$$f_{P-P}(\boldsymbol{r}_e,\boldsymbol{r}_h) = \frac{1}{\sqrt{N(\beta_{PP})}}e^{-\beta_{PP}|\boldsymbol{r}_e-\boldsymbol{r}_h|}\psi_P(\boldsymbol{r}_e)\psi_P(\boldsymbol{r}_h) \quad (9)$$

Figure S10(b) below shows the energy of the lowest energy S-S exciton, parameterized by the exciton binding energy B_x, versus the edge length, L, parameterized by exciton radius, a_x, for a cube-shaped NC. The black curve corresponds to the intermediate confinement limit (CL) and is calculated using Eq.7 with variational ansatz Eq 6 within a parabolic band dispersion approximation. For comparison the figure also shows the energies calculated within the strong and the weak confinement approximations. (see Ref. 11). Panel (c) in the figure shows the corresponding calculations for the next optically allowed exciton state, P-P corresponding to the P to P transition in the diagram of panel (a). For reference, the energies for the S-S and P-P excitons in the strong and weak confinement limits are given in Table S8.

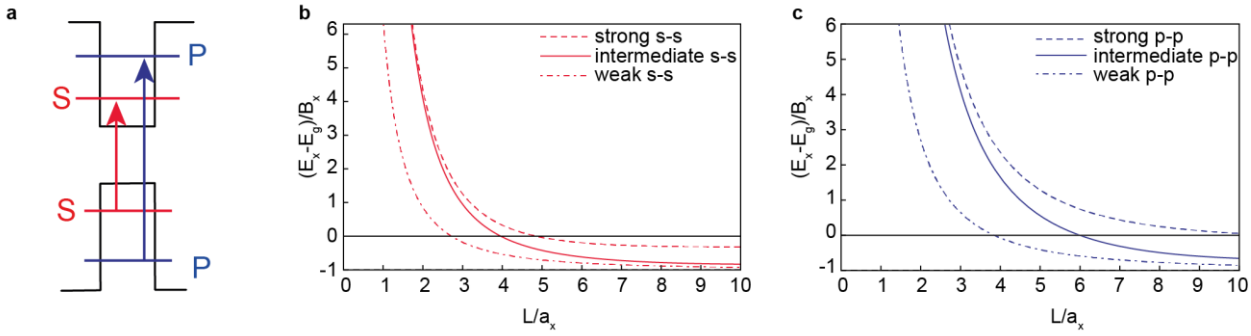

Figure S10. Optical transitions, (a), and exciton energies for the lowest energy S-S exciton, (b), and the P-P exciton, (c), for a cube-shaped NC. Panels (b) and (c) show exciton energies parameterized by the exciton binding energy, B_x, versus edge length L of a cube-shaped NC parameterized by the exciton radius, a_x. The intermediate CL result is calculated by variational optimization of Eq. 7 using ansatz function Eq.6 for the S-S exciton or Eq 9 for the P-P exciton. The strong CL calculation reflects the particle in a box quantization for electrons and holes with wavefunctions each given by Eq. 5 with Coulomb correction evaluated in first order perturbation theory. The weak confinement result reflects center-of-mass quantization of the exciton as a whole, described using Eq. 5, and relative motion described by the 1s hydrogenic wavefunction, with exciton binding energy B_x. Calculations shown here are performed within the parabolic band dispersion approximation with equal electron and hole effective masses, $m_e = m_h$.

Table S9. Energy of the S-S and P-P excitons for a cube-shaped NC of edge length L, in the strong and weak confinement limits, within the parabolic band approximation. The exciton radius, $a_x = a_0 \varepsilon m_0/\mu$, where a_o is the hydrogen Bohr radius, , m_0 is the free electron mass, $\mu = \left(\frac{1}{m_e} + \frac{1}{m_h}\right)^{-1}$ is the exciton reduced effective mass, and the bulk exciton binding energy $\boldsymbol{B_x} = \frac{\mu}{\boldsymbol{m_0 \epsilon_{eff}}^2}\boldsymbol{Ry} = \frac{\hbar^2}{2\mu a_x^2} = \frac{1}{2}\frac{e^2}{\epsilon_{eff}\, a_x}$, where Ry is the Rydberg. The numerical factors within the Coulomb energy term for the strong confinement approximation represent the result of numerical integration of the Coulomb energy within first-order perturbation theory. In the table $M = m_e + m_h$ is the total exciton mass.

	S-S exciton	P-P exciton
Strong confinement	$E_x = E_g + B_x \left\{ 3\left(\frac{\pi}{L/a_x}\right)^2 - 2\left(\frac{3.047}{L/a_x}\right) \right\}$	$E_x = E_g + B_x \left\{ 6\left(\frac{\pi}{L/a_x}\right)^2 - 2\left(\frac{2.705}{L/a_x}\right) \right\}$
Weak confinement	$E_x = E_g + B_x \left\{ 3\frac{\mu}{M}\left(\frac{\pi}{L/a_x}\right)^2 - 1 \right\}$	$E_x = E_g + B_x \left\{ 6\frac{\mu}{M}\left(\frac{\pi}{L/a_x}\right)^2 - 1 \right\}$

Extension to non- cube shaped NCs. Here we generalize this approach to describe the exciton energy for NCs with a non-cube shape. We will subsequently further extend the approach to include the effect of band non-parabolicity, and will apply the approach not only to the lowest energy exciton, but to higher energy exciton states as well. We first re-write the expression for the lowest energy exciton wave function to describe the exciton in a rectangular prism of edge lengths L_x, L_y, L_z:

$$\psi_S(x,y,z) = \sqrt{\frac{8}{L_x L_y L_z}} \cos\left(\frac{\pi x}{L_x}\right) \cos\left(\frac{\pi y}{L_y}\right) \cos\left(\frac{\pi z}{L_z}\right) \tag{10}$$

Evaluating the energy we find that it can be written in the form

$$E_x = -\frac{\hbar^2}{2\mu {L_{eff}}^2}\frac{I_K}{N} + \frac{e^2}{\epsilon_{eff}\, L_{eff}}\frac{I_C}{N} \tag{11}$$

In this expression, $\mu = \left(\frac{1}{m_e} + \frac{1}{m_h}\right)^{-1}$ is the exciton reduced effective mass, I_K, I_C and N are dimensionless integrals for the kinetic and potential energies, and the normalization, respectively. These integrals are written in terms of dimensionless coordinates, $\boldsymbol{u_e} = \boldsymbol{r_e}/L_{eff}$ and $\boldsymbol{u_h} = \boldsymbol{r_h}/L_{eff,}$ where the effective length, $L_{eff,}$ is chosen as the edge length of a cube with the same kinetic energy for the lowest energy exciton. We now derive expressions for the effective length, $L_{eff,}$ and the integrals. Suppose that we know the ratios of the edge lengths in the form $r_x = L_x/L_{z,}$ $r_y = L_y/L_{z,}$ and $r_z = 1$ as in the SAXS measurement described in Figures 1 and S8 as well as Table S7 and the associated text. Then the requirement on the kinetic energy of the ground exciton can be written,

$$\left(\frac{3}{{L_{eff}}^2}\right) = \frac{1}{{L_z}^2}\left(1 + \frac{1}{r_x^2} + \frac{1}{r_y^2}\right) \tag{12}$$

which leads to an expression for the effective length in terms of the reference edge length, $\boldsymbol{L_z}$:

$$L_{eff} = L_z\sqrt{3/\left(1 + \frac{1}{r_x^2} + \frac{1}{r_y^2}\right)} \tag{13}$$

It is important to note that effective length $\boldsymbol{L_{eff}}$ is very close to the average length $\boldsymbol{L_{ave} = L_z\,(1 + r_x + r_y)/3}$. For example, for NCs with an aspect ratio 1:1.2:1.2, as described in the main text, $\boldsymbol{L_{ave}/\,L_z = 1.13}$ while $\boldsymbol{L_{eff}/\,L_z = 1.12}$ for the same aspect ratio. The difference between $\boldsymbol{L_{eff}}$ and $\boldsymbol{L_{ave}}$ for a 10 nm size NC amounts to only 0.2 nm, well with experimental uncertainty. As a result, calculations in terms of $\boldsymbol{L_{eff}}$ can be directly compared to measured sizing curves with average sizes independent of the means of their acquisition. When $\boldsymbol{L_{eff}}$ is used as ordinate, models of NCs with different orthorhombic shapes could be directly compared.

Defining the ratios $\boldsymbol{l_x = L_x/L_{eff,}}$ $\boldsymbol{l_y = \frac{L_y}{L_{eff}}}$, $\boldsymbol{l_z = L_z/L_{eff}}$, we then rewrite the ground exciton base function Eq.10 as,

$$\psi_S(x,y,z) = \frac{1}{{L_{eff}}^{\frac{3}{2}}}\sqrt{\frac{8}{l_x l_y l_z}}\cos\left(\frac{\pi x}{L_{eff}\ l_x}\right)\cos\left(\frac{\pi y}{L_{eff}\ l_y}\right)\cos\left(\frac{\pi z}{L_{eff}\ l_z}\right) \tag{14}$$

To perform the integrals we need to write this in dimensionless form in terms of $= \boldsymbol{r}/L_{eff}$:

$$\psi_S(u_x, u_y u_z) = \sqrt{\frac{8}{l_x l_y l_z}}\cos\left(\frac{\pi u_x}{l_x}\right)\cos\left(\frac{\pi u_y}{l_y}\right)\cos\left(\frac{\pi u_z}{l_z}\right) \tag{15}$$

As a result, the ansatz function for the lowest energy S-S exciton transforms to,

$$f_{S-S}(\boldsymbol{u_e}, \boldsymbol{u_h}) = \frac{1}{\sqrt{N(b)}} e^{-b|\boldsymbol{u_e} - \boldsymbol{u_h}|}\psi_S(\boldsymbol{u_e})\psi_S(\boldsymbol{u_h}) \tag{16}$$

where we have used $b = \beta\, L_{eff}$. In terms of this dimensionless function, the dimensionless kinetic energy integral becomes,

$$I_K = I_K(b) = \int_{-\frac{l_x}{2}}^{\frac{l_x}{2}}\int_{-\frac{l_y}{2}}^{\frac{l_y}{2}}\int_{-\frac{l_y}{2}}^{\frac{l_y}{2}} d^3\,\boldsymbol{u_e} \int_{-\frac{l_x}{2}}^{\frac{l_x}{2}}\int_{-\frac{l_y}{2}}^{\frac{l_y}{2}}\int_{-\frac{l_y}{2}}^{\frac{l_y}{2}} d^3\,\boldsymbol{u_h}\ f_{S/S}(\boldsymbol{u_e}, \boldsymbol{u_h})\ \nabla^2_{\boldsymbol{u_e}}\ f_{S-S}(\boldsymbol{u_e}, \boldsymbol{u_h}) \tag{17}$$

The Coulomb integral, I_C, is

$$I_C = I_C(b) = \int_{-\frac{l_x}{2}}^{\frac{l_x}{2}}\int_{-\frac{l_y}{2}}^{\frac{l_y}{2}}\int_{-\frac{l_y}{2}}^{\frac{l_y}{2}} d^3\,\boldsymbol{u_e} \int_{-\frac{l_x}{2}}^{\frac{l_x}{2}}\int_{-\frac{l_y}{2}}^{\frac{l_y}{2}}\int_{-\frac{l_y}{2}}^{\frac{l_y}{2}} d^3\,\boldsymbol{u_h}\ \frac{1}{|\boldsymbol{u_e} - \boldsymbol{u_h}|}\ |f_{S-S}(\boldsymbol{u_e}, \boldsymbol{u_h})|^2 \tag{18}$$

while N(b), the normalization integral, is written in terms of the dimensionless function as,

$$N = N(b) = \int_{-\frac{l_x}{2}}^{\frac{l_x}{2}}\int_{-\frac{l_y}{2}}^{\frac{l_y}{2}}\int_{-\frac{l_y}{2}}^{\frac{l_y}{2}} d^3\,\boldsymbol{u_e} \int_{-\frac{l_x}{2}}^{\frac{l_x}{2}}\int_{-\frac{l_y}{2}}^{\frac{l_y}{2}}\int_{-\frac{l_y}{2}}^{\frac{l_y}{2}} d^3\,\boldsymbol{u_h}\ |f_{S-S}(\boldsymbol{u_e}, \boldsymbol{u_h})|^2 \tag{19}$$

It should be noted here that the normalization integral, N, plays a key role in determining the exciton oscillator strength, which can be shown to be given by, [9]

$$f(L_{eff}) = \frac{f_o}{N(b_{opt}(L_{eff}))} \tag{20}$$

where $f_o = E_p/\hbar\omega$, with E_p denoting the Kane energy and $\hbar\omega$ the transition energy.

Intermediate confinement model with band non-parabolicity. In Ref. 12, Sercel *et al.* showed that even with the variational approach described above, the parabolic band approximation does not yield a good description of the size dependence of the measured[13] lowest energy exciton energies in $CsPbBr_3$ NCs. The reason for the discrepancy was found to be band non-parabolicity not accounted for in the parabolic band approach described by Becker *et al.* [9] To account for non-parabolicity effects, Sercel *et al.*[12] used a 2-band Kane model to derive an expression for the energy dependent effective mass and showed that the non-parabolic model provides a good description for the NC size dependent energy of the lowest exciton absorption line for cube shaped NCs. A similar study conducted on absorption data from $CsPbI_3$ NCs in Ref.14 using the model of Ref. 12 reached the same conclusion. The result is that the exciton reduced mass μ in Eq. 11 is replaced by an energy dependent reduced mass, μ', ($\mu' = \frac{m'}{2}$ where m' is the non-parabolic carrier mass which is approximately the same for the electron and the hole). The energy dependent carrier effective mass can be expressed as a function of L_{eff}, as shown in Sercel *et al.*, Ref. 12:

$$\frac{m'}{m_0} = \frac{3\left\{\sqrt{E_g^2 + \frac{2\,E_p}{m_0}\hbar^2\left(\frac{\pi}{L_{eff}}\right)^2} + \sqrt{E_g^2 + \frac{4E_p}{m_0}\hbar^2\left(\frac{\pi}{L_{eff}}\right)^2}\right\}}{2E_p} \tag{21}$$

In this expression, E_g is the bulk band gap, and E_p is the Kane energy, $E_p = 2\,|P|^2/m_e$, where P is the Kane momentum matrix element, and m_e is the free electron mass. It was also shown in Ref. 12 that to a good approximation, the lowest exciton energy calculated with the variational approach of Eq. 11 can be expressed in terms of the strong confinement result with an approximate Coulomb correction, written in terms of the bulk exciton radius, $a_x = a_0\varepsilon/\mu$, where $a_0$is the hydrogen Bohr radius, and the bulk exciton binding energy $B_x = \frac{\mu}{\epsilon^2}Ry = \frac{\hbar^2}{2\mu a_x^2}$, where Ry is the Rydberg:

$$E_x \approx E_g + \frac{\hbar^2}{2\mu'}\frac{3\pi^2}{L^2} - B_x\sqrt{1 + \left\{2 \times 3.047\left(\frac{a_x}{L}\right)\right\}^2} \tag{22}$$

Application of the method to higher energy exciton states. Having developed the framework for describing the lowest energy exciton states in a rectangular prismatic NC in the intermediate confinement regime, we now extend the method to the description of higher lying exciton states. We will focus on higher energy states which involve "P" type envelope functions with one nodal plane in either the electron or the hole wavefunction. As shown in Ref.12, the energy dependent effective mass for such P-like states is identical to that developed for the S-like exciton, Eq. 21, owing to the fact that while an S-like state in the conduction or valence band couples to a P like state in the opposite band, the converse is true, that is, a P-like state in the conduction or valence band couples to a S- like state in the opposite band. To evaluate the exciton energy for such P-like excitons we simply need to modify the expression for the base carrier wavefunction given for the S state in Eq. 14. The P_x, P_y, and P_z base functions are given by,

$$\psi_{P_x}(x,y,z) = \frac{1}{{L_{eff}}^{\frac{3}{2}}}\sqrt{\frac{8}{l_x l_y l_z}}\sin\left(\frac{2\pi x}{L_{eff}\ l_x}\right)\cos\left(\frac{\pi y}{L_{eff}\ l_y}\right)\cos\left(\frac{\pi z}{L_{eff}\ l_z}\right) \tag{23}$$

$$\psi_{P_y}(x,y,z) = \frac{1}{{L_{eff}}^{\frac{3}{2}}}\sqrt{\frac{8}{l_x l_y l_z}}\cos\left(\frac{\pi x}{L_{eff}\ l_x}\right)\sin\left(\frac{2\pi y}{L_{eff}\ l_y}\right)\cos\left(\frac{\pi z}{L_{eff}\ l_z}\right) \tag{24}$$

$$\psi_{P_z}(x,y,z) = \frac{1}{{L_{eff}}^{3/2}}\sqrt{\frac{8}{l_x l_y l_z}}\cos\left(\frac{\pi x}{L_{eff}\ l_x}\right)\cos\left(\frac{\pi y}{L_{eff}\ l_y}\right)\sin\left(\frac{2\pi z}{L_{eff}\ l_z}\right) \tag{25}$$

Using these we can construct ansatz functions and carry out the variational procedure just as we did for the lowest energy S-S exciton state. For example we can construct the wavefunctions for the dipole active P_x/ P_x, P_y/ P_y, P_z/ P_z excitons as follows: Writing the index *i* as a stand-in for x, y, z,

$$f_{P_i-P_i}(\boldsymbol{u}_e,\boldsymbol{u}_h) = \frac{1}{\sqrt{N(b)}}e^{-b|\boldsymbol{u}_e-\boldsymbol{u}_h|}\psi_{P_i}(\boldsymbol{u}_e)\psi_{P_i}(\boldsymbol{u}_h) \tag{26}$$

Using this ansatz function, again the energy, Eq. 7 is evaluated and minimized with respect to the variational parameter. Optically inactive states can be formed using combinations such as S/P_x or P_x/S and for a total of 6 similar variations:

$$f_{S-P_i}(\boldsymbol{u}_e,\boldsymbol{u}_h)=\frac{1}{\sqrt{N(b)}}e^{-b|\boldsymbol{u}_e-\boldsymbol{u}_h|}\psi_S(\boldsymbol{u}_e)\psi_{P_i}(\boldsymbol{u}_h)$$
$$f_{P_i-S}(\boldsymbol{u}_e,\boldsymbol{u}_h)=\frac{1}{\sqrt{N(b)}}e^{-b|\boldsymbol{u}_e-\boldsymbol{u}_h|}\psi_{P_i}(\boldsymbol{u}_e)\psi_S(\boldsymbol{u}_h) \quad (27)$$

There are also other optically inactive combinations involving combinations of P_i/ P_j with $i \neq j$, for 6 variations, with a total of 2 nodal planes between the electron and the hole wavefunctions, such as,

$$f_{P_i-P_j}(\boldsymbol{u}_e,\boldsymbol{u}_h)=\frac{1}{\sqrt{N(b)}}e^{-b|\boldsymbol{u}_e-\boldsymbol{u}_h|}\psi_{P_i}(\boldsymbol{u}_e)\psi_{P_j}(\boldsymbol{u}_h), i\neq j \quad (28)$$

Defining other base functions with two nodal planes, such as,

$$\psi_{P_yP_z}(x,y,z)=\frac{1}{{L_{eff}}^{3/2}}\sqrt{\frac{8}{l_xl_yl_z}}\cos\left(\frac{\pi x}{L_{eff}\ l_x}\right)\mathrm{Sin}\left(\frac{2\pi y}{L_{eff}\ l_y}\right)\sin\left(\frac{2\pi z}{L_{eff}\ l_z}\right) \quad (29)$$

We can construct dark states like the following with of a total of two nodal planes for the electron or the hole, of which there are 6 possible variations:

$$f_{S-P_jP_k}(\boldsymbol{u}_e,\boldsymbol{u}_h)=\frac{1}{\sqrt{N(b)}}e^{-b|\boldsymbol{u}_e-\boldsymbol{u}_h|}\psi_{P_i}(\boldsymbol{u}_e)\psi_{P_jP_k}(\boldsymbol{u}_h) \quad (30)$$

We can construct dark states like the following with of a total of three nodal planes between the electron and hole, of which there are 12 possible variations whose degeneracies would be split in a non-cube shaped NC:

$$f_{P_i-P_jP_k}(\boldsymbol{u}_e,\boldsymbol{u}_h)=\frac{1}{\sqrt{N(b)}}e^{-b|\boldsymbol{u}_e-\boldsymbol{u}_h|}\psi_{P_i}(\boldsymbol{u}_e)\psi_{P_jP_k}(\boldsymbol{u}_h) \quad (31)$$

Calculated results for the optically active S-S and P-P exciton states. For comparison to the measured exciton absorption spectra shown in Figure 3a we first calculated the energy of the lowest energy, S-S, exciton and the higher energy optically active P-P exciton in a cube shaped NC as shown in Figure S11, panel (a). This calculation was performed as described above for a cube shape, with the materials parameters determined by best fit to the absorption energy data in Figure 3a and are given in the caption of Figure S11. As described in the main text, the $CsPbBr_3$ NCs in this study have anisotropic shapes as determined using the SAXS technique (Figures 2b,S8 and Table S7). Inspection of the results in Table S7 shows that the NCs have a shape which is closely approximated by a cuboid with 2 equal edge lengths in the ratios $r_x : r_y : r_z$ equal to r : r : 1 with r = 1.2, independent of size.

Figure S11a shows the calculated exciton energies for this case, showing the expected result that the optically active P_z/ P_z exciton, which nodal planes perpendicular to the short axis of the NCs, shifts to higher energy in relation to the degenerate P_x/ P_x and P_y/ P_y states whose nodal planes contain the short axis. Figure S11b shows the splitting between the P_z/ P_z exciton and the P_x/ P_x ; P_y/ P_y degenerate pair plotted for several NC sizes versus (r^{-1}) where r is the aspect ratio r:r:1 of a cuboidal NC. The calculation shows that the P-state splitting is linear in the aspect ratio over the range 1 to 1.3. In Figure S12 we show the calculated exciton states including, in addition to the optically active exciton levels shown in Figure S11, the "dark", or dipole inactive exciton states described by Eqs. 27, 28, and 30. For the higher lying dark states described by Eq 28 and 30 the aspect ratio *r* was taken as *r = 1* for simplicity.

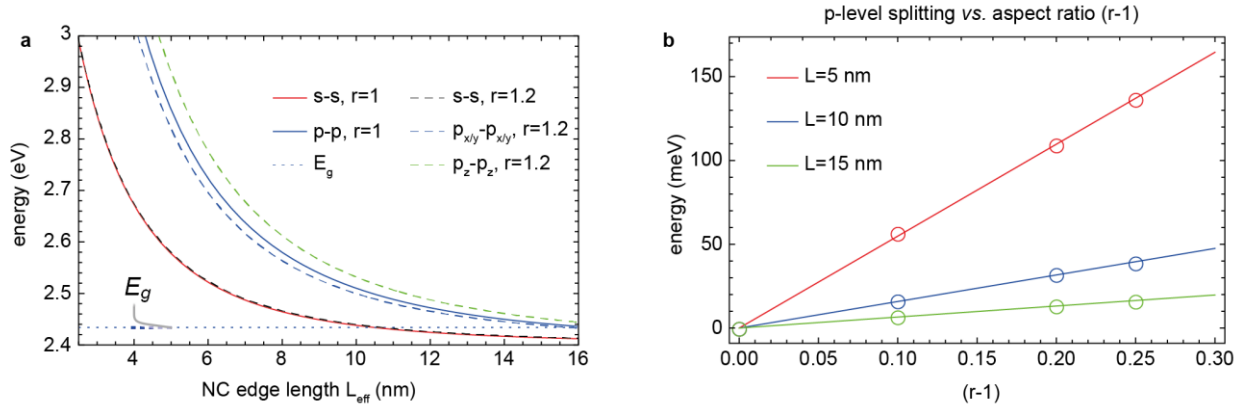

Figure S11. Energies of the lowest energy S-S exciton and the higher energy optically active exciton states P_x-P_x, P_y-P_y, and P_z-P_z , versus the effective edge length L_{eff} , panel (a) ; and panel (b), the splitting between the P_z-P_z exciton

and the P_x-P_x, P_y-P_y degenerate pair plotted for several sizes versus (r-1) where r is the aspect ratio r:r:1 of the cuboidal NC. In panel (a) the solid lines are calculated for a cube-shaped NC, r = 1, while the dashed lines are calculated for cuboids with r = 1.2. In panel(b), The calculated points are shown as open circles while the solid lines are linear fits through the calculated points. In all cases, the energies are calculated in the intermediate confinement limit by variational optimization of Eq. 7 using the appropriate ansatz functions; namely, Eq. 16 for the S-S exciton and Eq. 26 for the P-P excitons. Parameters used in the calculation are E_g = 2434.2 meV, E_p = 26494.4 meV, and ϵ_{eff} = 7.3.

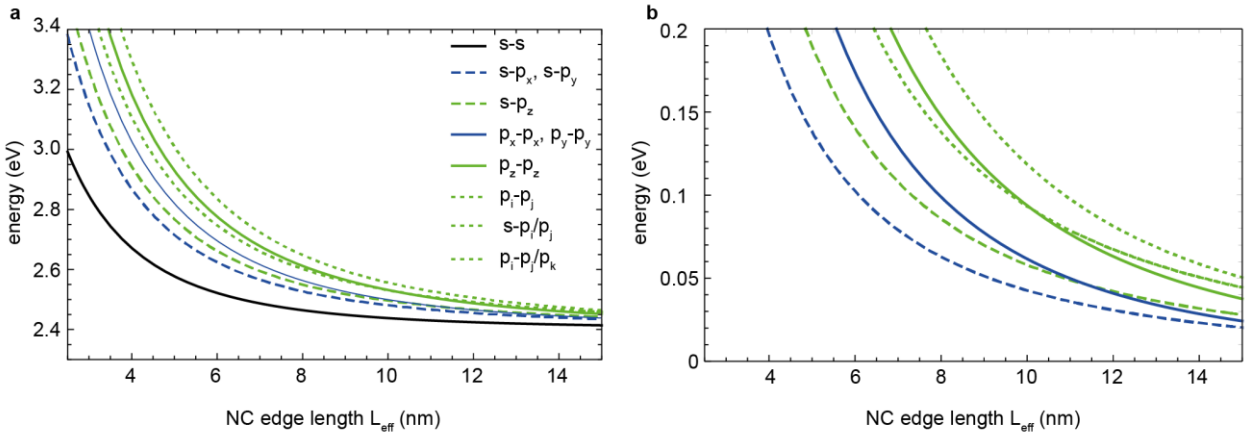

Figure S12. Exciton energies versus the effective edge length L_{eff} for a NC with cuboidal shape, with aspect ratio r:r:1, with r= 1.2. Panel (a) shows the absorption energy of each state; while panel (b) shows the energy of the higher energy states relative to the lowest exciton energy level. In the figure, the solid lines depict optically active excitons, while the dashed and dotted lines correspond to dipole inactive exciton levels. The lowest energy S-S exciton is calculated using, Eq. 16 while the P-P excitons are calculated using Eq. 26. The dark states denoted S-P_x, S-P_y and S-P_z are calculated using Eq. 27. The other excited states S-P_iP_j and P_i-P_jP_k are calculated using Eq 30 and 31 respectively, for aspect ratio *r =1*. Materials parameters used in the calculation are the same as in Figure S11.

Fitting procedure and results. We compared the model developed above to the measured energies for the two lowest energy exciton transitions. One issue to be addressed is the potential role of fine structure splitting in making this comparison. The lowest energy exciton level, S-S, is not split by the shape anisotropy apart from fine structure effects which give rise to splitting in the meV range,[11, 12] which is much less than either the inhomogeneous linewidth or the homogenous linewidth of the exciton transition at room temperature, which is known to be of order 100 meV.[15] Consequently the shape-dependent fine structure splitting is neglected in our calculations. Second, in order to compare the model developed to the experimental data, we must know the bulk band gap, E_g, the effective mass, which is determined by the band gap and the Kane energy, E_p, and finally, the effective dielectric ϵ_{eff} which screens the electron/hole Coulomb interaction. For the bulk material, the effective mass is related to the bandgap and the Kane energy by $m = \frac{3\,E_p}{E_g}$; however, for small NCs, it is important to account for band non-parabolicity, which was done in our calculations using Eq. 21 for the energy dependent effective mass. Calculations were performed using the intermediate confinement model for the S-S exciton represented by variational optimization of the exciton energy, Eq. 7, using the ansatz function, Eq. 16, for the S-S exciton. The upper P-P transition energies were calculated using ansatz functions given by Eq. 26. Starting materials-parameters were chosen using the room temperature corrected values of the effective mass of bulk $CsPbBr_3$ as determined via magneto-transmission measurements in Ref. 16. The data points used for fitting are plotted in Figure 3c. Only the S-S transitions were used for fitting. The spectral transitions were obtained from the first excitonic absorption peak (minima in the second derivative of the measure solution spectrum). The shape and size information were obtained from SAXS data, for a valid comparison the maxima in the volume distribution were used as edge lengths (absorption scales with volume).

We used the "NonlinearModelFit" routine in Mathematica to carry out a nonlinear optimization of the material-parameters to match the model to the lowest exciton absorption energy versus the measured NC size. The room temperature bulk bandgap was constrained in these fits to reproduce the bulk exciton absorption peak energy measured at room temperature,[12] according to the formula,

$$E_{ex} = E_g - B_x \tag{32}$$

where $B_x = \frac{\mu}{{m_0\epsilon_{eff}}^2} Ry = \frac{\hbar^2}{2\mu a_x^2}$ is the bulk exciton binding energy, and the reduced mass μ is given for the bulk in terms of the Kane energy, E_p, and the band gap, E_g, by $\mu = \frac{3}{2}\frac{E_p}{E_g}$. The effective dielectric ϵ_{eff} was constrained to the value determined by the magneto-transmission measurements of Yang *et al.*[16] Once the materials parameters were optimized in this fashion, the energies of the S-S, P_x-P_x, P_y-P_y, and P_z-P_z excitons were calculated and overlaid against the measured data, as shown in Figure S13 and Figure 3c. In addition to the data set for which sizes were determined using SAXS, two additional data sets are included in Figure S13: For one dataset, average edge lengths were measured using TEM, and for the other, the effective edge length was calculated using the intermediate confinement model for the S-S exciton from the measured lowest energy exciton energy.

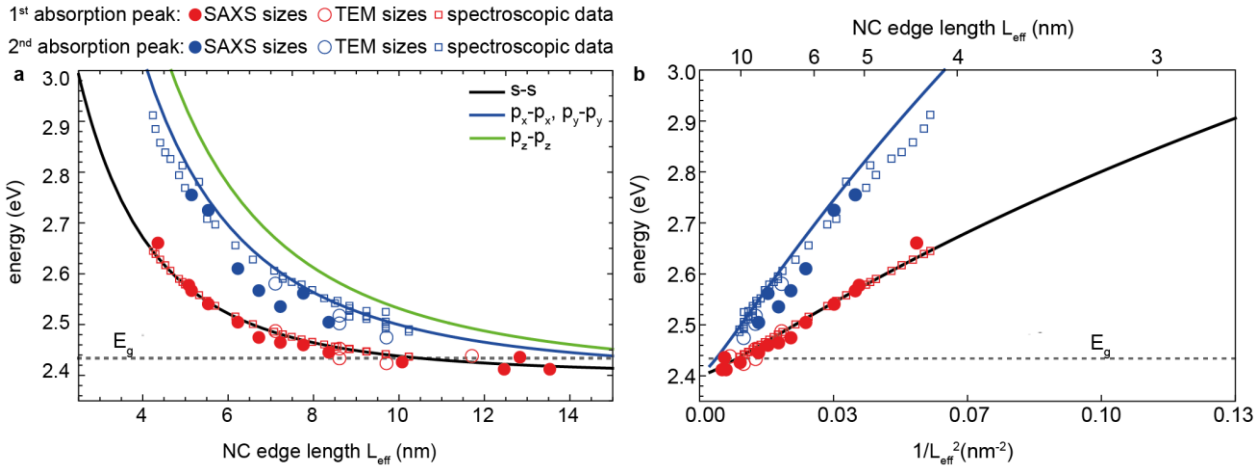

Figure S13. Comparison of the calculated SS and PP exciton energies against the effective length L_{eff}, panel (a), and the inverse square of the effective edge length, panel (b), for nanocrystals with aspect ratio r : r : 1, with r = 1.2 as determined by SAXS measurements. Solid circles show data for which the size was determined by SAXS. Also shown on this plot are additional measured data with average edge lengths measured by TEM, open circles; and data for which the effective size was calculated from the S-S absorption peak energy using the intermediate confinement model for the SS exciton. Parameters used in the calculation are E_g = 2434.2 meV, E_p = 26494.4 meV, determined by non-linear fitting to the 1st excitonic peak energy for the SAXS dataset with the effective dielectric constrained to the measured bulk value and ϵ_{eff} = 7.3. Within the P-P exciton grouping, the P_x-P_x, P_y-P_y states and the P_z-P_z are split due to the NC shape anisotropy, see Figure S11.

The measured data correspond reasonably well to the model calculation for the lower degenerate pair P_x-P_x and P_y-P_y within the PP manifold, although the calculated energies are higher than the measured energies for the smallest NCs. To understand why the measured 2nd excitonic peaks may correspond in energy to the lower line within the PP manifold, we note that while the P-P exciton transition is split, by up to ~ 100 meV for NCs with effective sizes of ~ 5nm and an aspect ratio r = 1.2, this splitting is comparable to or less than the homogenous linewidth expected for the transition. As a result, the PP doublet is not expected to be resolved at room temperature. In the present case the doublet is comprised of a lower transition twice as strong as the upper transition. This is illustrated in **Figure S14a**. With an unresolved doublet, peak finding procedures that find either the peak maximum or the minimum in the second derivative **Figure S14b** will return the energy of the lower energy transition. As such we expect the measured 2nd excitonic peak energies to correspond to the model for the lower degenerate pair P_x-P_x and P_y-P_y rather than the upper exciton, P_z-P_z.

We also considered several possible explanations for why the calculated energies for the P_x-P_x and P_y-P_y exciton are somewhat larger than the measured PP-P absorption peak energies for the smallest NCs. First, inspection of the measured aspect ratios in **Table S7** indicates a slight increase in the aspect ratio for the smaller sized NCs, which is not accounted for in the model. The larger aspect ratio *r* for small-sized NCs would tend to push the lower P_x-P_x and P_y-P_y states downwards in energy. However, the magnitude of this effect is not large enough to account for the

difference between the model curve and the measured P-P absorption peak energies, nor is the trend significant with respect to the error of the measurement. More likely, the discrepancy between the model and the data for small sized NC is due to finite barrier effects that are not accounted for in the model, or fine structure splitting, which increases roughly as the inverse of the size cubed, also not accounted for in the model.

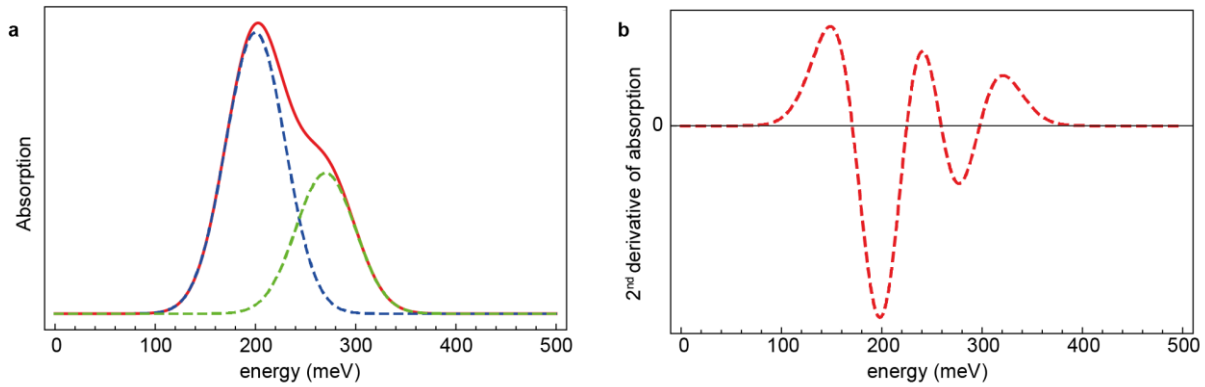

Figure S14. Illustration of line shape of the P-P exciton transition, comprised of a lower energy degenerate doublet separated by shape dependent splitting from an upper singlet line. The spectrum shown is calculated assuming a Gaussian linewidth for each transition, with the energy separation between the transitions equal to their full width at half maximum (FWHM). The negative side peak in the second derivative of the spectrum occurs at the energy of the lower transition.

Sensitivity analysis. We performed a sensitivity analysis on the materials-parameters obtained by fitting the SAXS data set to the intermediate confinement model for the SS exciton. In **Figure S15** we show a comparison of the measured data for the 1st and 2nd excitonic peak energies with sizes measured by SAXS and by TEM, against the intermediate confinement model as before, but have overlaid model calculations with +/-10% variation in the effective dielectric and in the value of the Kane energy determined by fitting. Inspection of the plot indicates that 10% variation is about the limit of our ability to discriminate the parameter values. Indeed the 1-sigma uncertainty in the Kane energy determined by fitting is 4.5%.

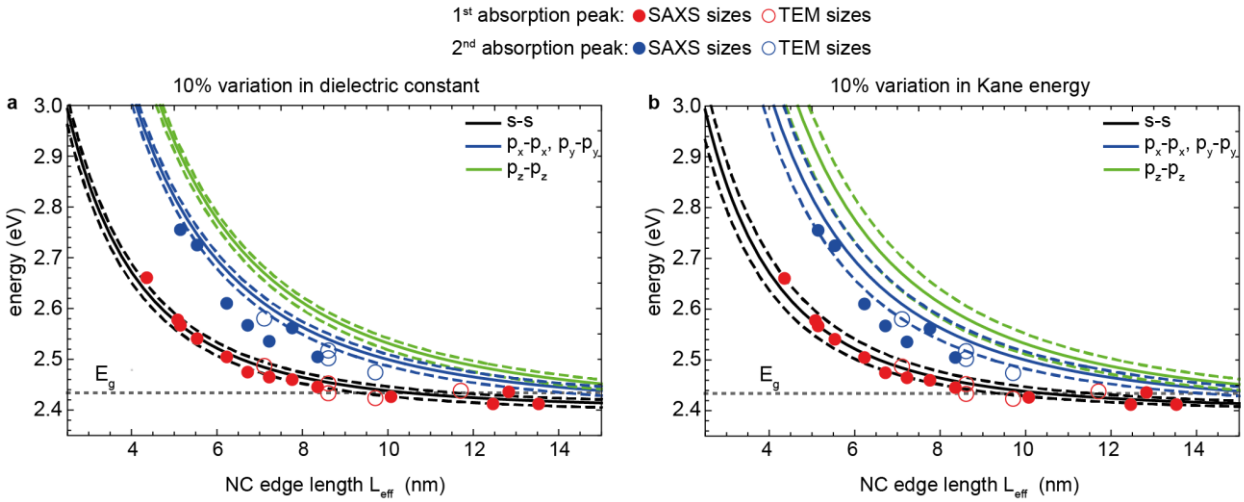

Figure S15. Sensitivity of the calculated S-S and P-P exciton energies against variation in model parameters. Plots show the exciton energies against the effective length L_{eff}. Panel (a) and panel (b) are calculated as in Figure S12, but with dashed lines depicting +/- 10% variation in the effective dielectric constant, panel (a), and in the Kane energy, panel(b). Solid (open) circles show data for which the size was determined by SAXS (TEM).

We also examined the sensitivity of the calculated S-S and P-P exciton energies against the degree of electron/hole correlation: That is, we compared the calculated results for the strong confinement approximation for which correlation

in the motion of the electron and the hole is neglected, to the intermediate confinement result as shown in Figure S13. This comparison is shown in Figure S15. In panel (a) the solid lines are calculated for intermediate confinement, as in Figure S13, but with the additional dashed lines depicting calculation for the corresponding exciton states within the strong confinement limit (SCL), which neglects correlated motion of the electron and the hole. The SCL calculation systematically overestimates the exciton energies relative to the intermediate confinement model and the data. In panel (b) the SCL calculation is repeated with a bandgap renormalization of 15 meV to account for exciton binding. The SS exciton energy calculated within the SCL reproduces the intermediate CL result with this bandgap renormalization, but the PP exciton states still systematically overshoot the intermediate CL model and the data.

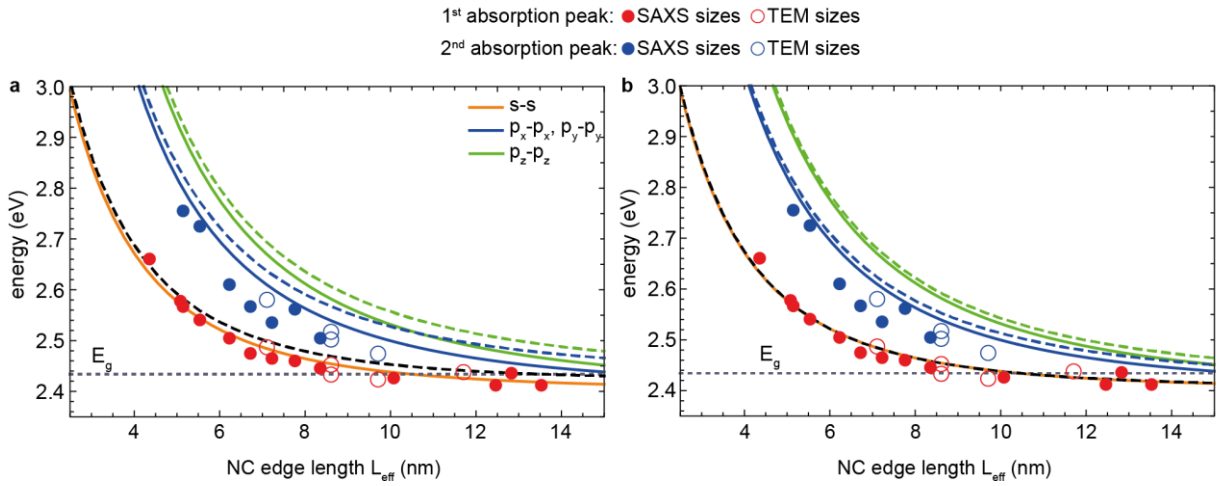

Figure S16. Sensitivity of the calculated S-S and P-P exciton energies against electron/hole correlation. Plots show the exciton energies against the effective length L_{eff}. Solid (open) circles show data for which the size was determined by SAXS (TEM). In panel (a) the solid lines are calculated for intermediate confinement, as in Figure S13, but with the additional dashed lines depicting calculation for the corresponding exciton states within the strong confinement limit (SCL), which neglects correlated motion of the electron and the hole. The SCL calculation systematically overestimates the exciton energies relative to the intermediate confinement model and the data. In panel (b) the SCL calculation is repeated with an ad-hoc bandgap renormalization of 15 meV to reflect exciton binding. In this case the S-S exciton energy calculated within the SCL with the bandgap renormalization reproduces the intermediate CL result, but the P-P exciton states are still systematically higher than the result calculated within the intermediate CL model.

Model for room temperature PL lifetime measurements. Having developed a model for the higher energy excitons in the $CsPbBr_3$ NCs we are in a position to model dynamic effects. We applied the model developed above, as reflected in Figure S12, to calculate the thermalized radiative recombination lifetime assuming that the exciton levels at room temperature are populated according to Boltzmann distribution and compared them to radiative PL-lifetimes measured for NCs of different sizes.
The working equation is:

$$\tau_{eff}(T) = \frac{\sum_i e^{-E_i/k_bT}}{\sum_i \left(\frac{1}{\tau_i}\right) e^{-E_i/k_bT}} \qquad (33)$$

Where the sum is taken over the exciton levels, *i*. That is, the effective lifetime is the population-weighted average of the reciprocal of the radiative decay rate taken over all the exciton states. The radiative transition rate for each state is proportional to its oscillator strength. As higher energy dark states are thermally populated, we expect the radiative lifetime to increase. This thermal population of upper dark states occurs more strongly for a given temperature for larger NCs where the energy level spacing is reduced (see Figure S12(b)). On the other hand, the oscillator strength of the NC is size dependent owing to the phenomenon of exciton giant oscillator transition strength. This phenomenon, first described for bound excitons at low temperatures[17] was recently confirmed to exist in $CsPbBr_3$ NCs by analysis of the size-dependence of the liquid helium temperature exciton radiative lifetimes, which are in the sub-ns range. [9] This effect tends to shorten the radiative lifetime as the size increases. The effective lifetime at a given temperature, for a given size, will be a tradeoff between these two competing effects.

Within the model developed above, for each exciton state, i, whose exciton wavefunction is written in the general form,

$$\psi_i = \frac{1}{\sqrt{N_i\left(b_{opt,i}(L_{eff})\right)}} e^{-b_i|\boldsymbol{u}_e - \boldsymbol{u}_h|} \psi_{i,e}(\boldsymbol{u}_e)\psi_{i,h}(\boldsymbol{u}_h) \tag{34}$$

the radiative lifetime is given by the expression: [9]

$$\left(\frac{1}{\tau_i(L_{eff})}\right) = \frac{4\,\omega n\,E_p}{9\cdot 137\,m_e\,c^2} D^2\,\frac{1}{N(b_{opt}(L_{eff}))} \equiv \left(\frac{\omega}{q}\right)\frac{1}{N(b_{opt}(L_{eff}))} \tag{35}$$

In this expression, ω is the angular frequency of the PL emission, n is the index of refraction of the medium surrounding the NC, E_p is the Kane energy, c is the speed of light, and m_e is the free electron mass. The factor D is the dielectric depolarization factor given approximately in terms of the dielectric constant of the medium, ϵ_{med} , and the high frequency dielectric constant of the NC, $\epsilon_{NC,\infty}$, by

$$D = \frac{3\epsilon_{med}}{2\epsilon_{med} + \epsilon_{NC,\infty}} \tag{36}$$

Giant oscillator strength comes about from the size dependent factor, $N\left(b_{opt}\left(L_{eff}\right)\right)$. computed for each state, i, whereas the parity selection rules come from the overlap, $\langle\psi_{e,i}|\psi_{hi}\rangle$, of the electron and hole components of the exciton base functions ψ_i. For example, for the SS exciton these are given for both the electron and the hole by Eq. 14. In the absence of electron/hole correlated motion, that is, in the strong confinement limit, this term is unity in the approximation that the NC surface is described by an infinite barrier.

In Figure S17, we compare the measured size dependent radiative lifetime at room temperature against results calculated within our model using Eq. 34 and 35, and fitting the constant factor q in Eq. 35 to match the measured lifetime for the smallest size NCs. We also show a calculation without the giant oscillator strength enhancement factor, that is, in Eq 35, the factor $N\left(b\left(L_{eff}\right)\right)$ is set to unity. Remarkably, the model which includes the GOS effect does *not* match the measured data at room temperature, while the model without the GOS effect matches the data quite closely. This is in distinct contrast to the situation at low temperature, where the GOS effect is crucial to understanding the faster radiative decay in larger sized NCs. [9] The explanation appears to be that at room temperature, PL emission probably involves de-cohered states in which the electron / hole correlation, which gives rise to the accumulation of oscillator strength responsible for GOS, is broken up by thermal scattering. On the other hand, a good description of absorption, being a prompt process, requires inclusion of the electron/hole correlation effect as indicated by the analysis in Figure S16. Further investigation of the mechanism of thermal quenching of the GOS effect, which governs PL emission at low temperature, [9] is in progress.

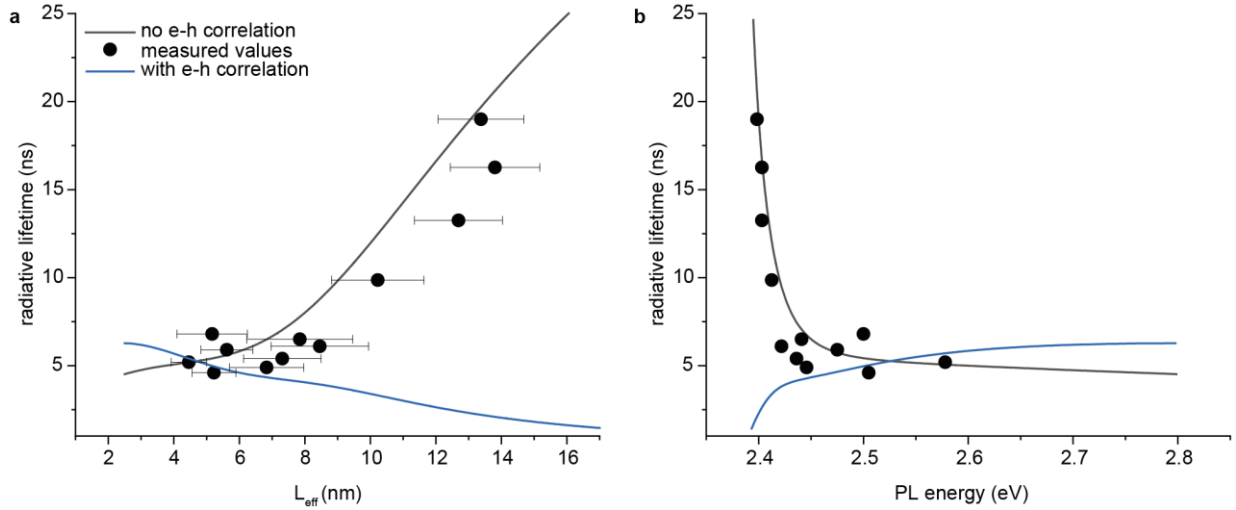

Figure S17. Effective radiative lifetime for $CsPbBr_3$ NCs measured as a function of size at room temperature and compared against results calculated within the intermediate confinement model, using Eq. 34 and 35, and the strong confinement model, in which the factor N in Eq. 35 is set to unity. The overlay was made without fitting other than to adjust the factor q in Eq 35 to match measured lifetime for small sized NCs. Panel (a) shows the comparison against measured NC size while panel (b) shows the lifetime plotted versus PL emission energy.

PREPARATION OF SUPERLATTICES

Preparation of cesium-oleate solution. Cs_2CO_3 (200 mg, 0.6 mmol) was mixed with octadecene (ODE, 7.5 mL) and oleic acid (OA, 0.6 mL) in a 100 mL-flask. The mixture was degassed three times at room temperature, heated to 120 °C for 10-15 min and left to cool down. The Cs-precursor solution was stored in a glove box.

Synthesis of OLA/OA-capped $CsPbBr_3$ NCs. $PbBr_2$ (55 mg, 0.15 mmol) was mixed with 5 mL distilled ODE in a 25 mL-flask. The mixture was heated to 180 °C under nitrogen atmosphere. When a temperature of *ca.* 120 °C was reached, 0.5 mL of dried OA and 0.5 mL distilled oleylamine (OLA) were injected. At 180 °C, 0.8 mL of the Cs-oleate solution was injected. After 10 s the reaction mixture was cooled down with a water-ice bath. The crude solution was centrifuged for 5 min at 20133 g. The resulting supernatant was discarded and the precipitate was dispersed in hexane (0.3 mL). The solution was centrifuged a second time for 3 min and the precipitate was discarded. The supernatant was isolated and diluted with additional hexane (0.3 mL) and centrifuged again for 10 min.

Colloidal solution of OAc/OAm-capped $CsPbBr_3$ NCs for the formation of SLs. 40 µl of NCs in hexane (obtained as described above) were mixed with 80 µl toluene, 0.5 µl OA and 0.5 µl OLA. This colloid was destabilized by adding 70 µl acetone, followed by centrifuging and dispersing in 0.1 mL anhydrous toluene.

Colloidal solution of ZI-$CsPbBr_3$ NCs for the formation of SLs. 20 µL of the as-prepared NC colloid (**3s**f2 or **3s**f4 NCs, 3mL) were dried under vacuum and then dissolved in 0.26 mL of anhydrous toluene.

Preparation of 3D-superlattices. $CsPbBr_3$ NC superlattices were grown on 5 mm × 5 mm silicon substrates. Shortly before the self-assembly process, the silicon substrate was purified in acetone and methanol, followed by the treatment with 4% solution of HF in water for 1-2 min and intensive washing in water. In a typical assembly process, the substrate was placed in a 10 mm × 10 mm × 10 mm Teflon well and 6 µl of NC toluene solution (see the solution preparation above) were spread onto the substrate. The well was covered with a glass slide and then the toluene was allowed to evaporate slowly within several hours.

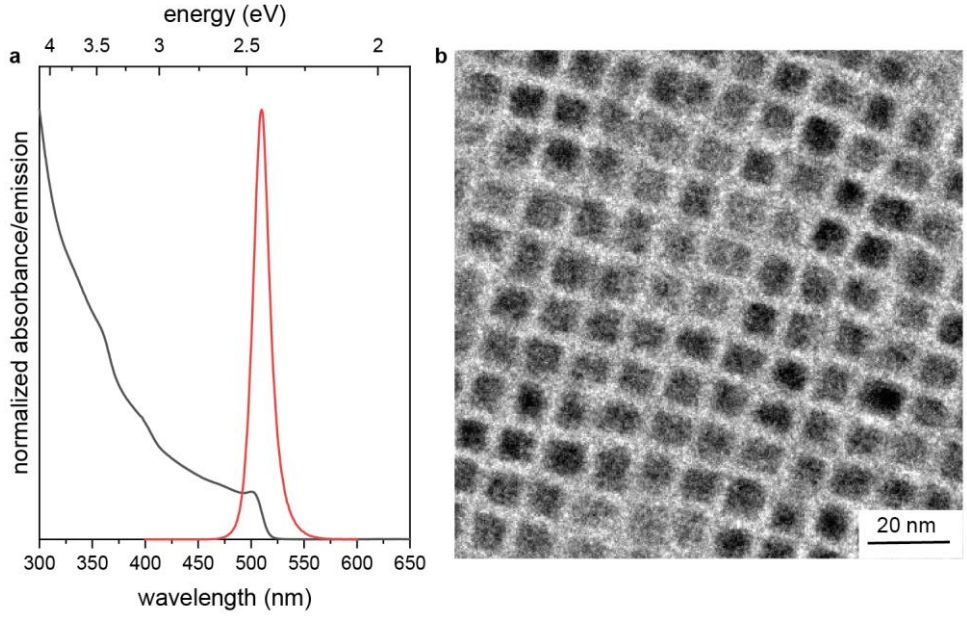

Figure S18. (a) Typical absorption and PL spectra for OLA/OA-capped $CsPbBr_3$ NCs used for self-assembly. (b) Corresponding low-resolution TEM image.

GRAZING INCIDENCE SMALL-ANGLE X-RAY SCATTERING

Grazing Incidence small-angle x-ray scattering (SAXS) measurements were performed at the Austrian SAXS beamline of the electron storage ring ELETTRA using a photon energy of 8 keV.[4] The beamline setup was adjusted to a sample to detector distance of approx. 1.8 m to result in an accessible q-range $q_V < 3.2$ nm^{-1} and $-1.2 < q_H < 2.4$ nm^{-1}, where q_V and q_H denote the vertical and horizontal scattering vector, respevtively. All images were recorded using the Pilatus3 1M detector (Dectris, Switzerland). All images were taken at an incidence angle of 0.20° (aligned by position of specular reflection) with a constant exposure time of 10 sec. Reference patterns to calibrate the q-scale were collected of silver-behenate (*d*-spacings of 5.838 nm). Conversion to q-space and calculation of horizontal cuts was performed using NIKA2D[18] while lattice indexing including q-space mapping was done using GIXSGUI.[19]

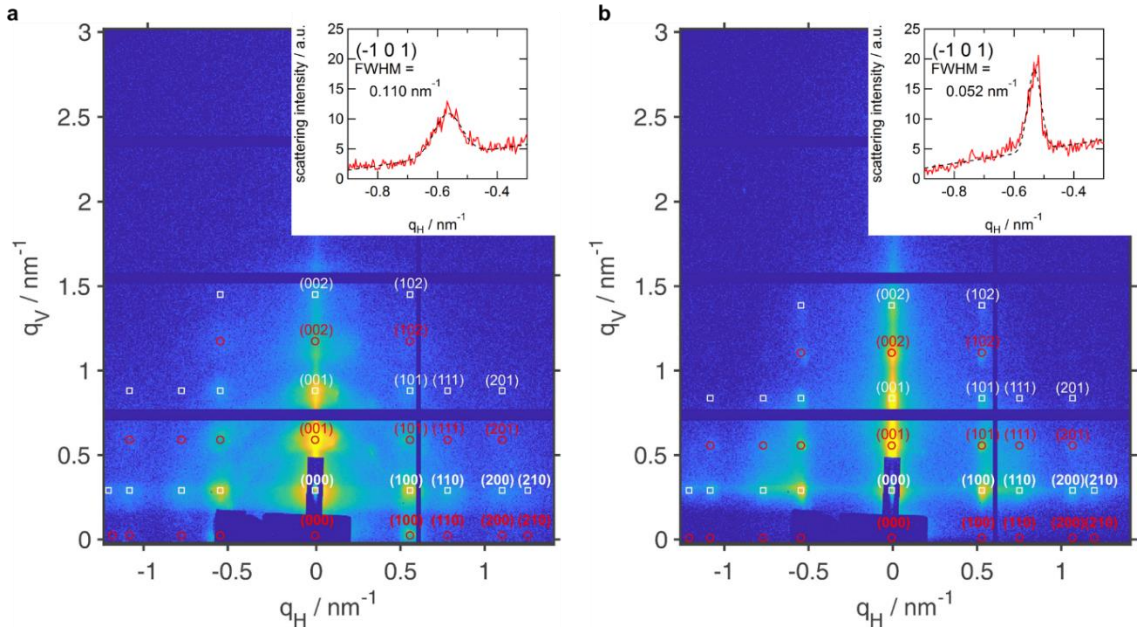

Figure S19. (a) GISAXS image of superlattices from OA/OLA-capped NCs, indexed with a tetragonal unit cells with a=b=11.4 nm and c=11.0 nm. (b) GISAXS image of superlattices from zwitterion-capped NCs (**4**sf2), indexed with a tetragonal unit cells with a=b=11.5 nm and c=11.3 nm. Note that white and red markers correspond to reflected and transmitted scattering contributions of the theoretical lattices, respectively. Insets show peak-fits of the ($\bar{1}$ 0 1) SL reflections to obtain the coherent scattering length (relating to the ordered domain size of the SLs). The obtained FWHMs of the scattering peaks relate to a mean coherent domain size of $2\pi/FWHM$ = 57.1 and 120.8 nm in case of OA/OLA- and zwitterion-capped NCs, respectively.

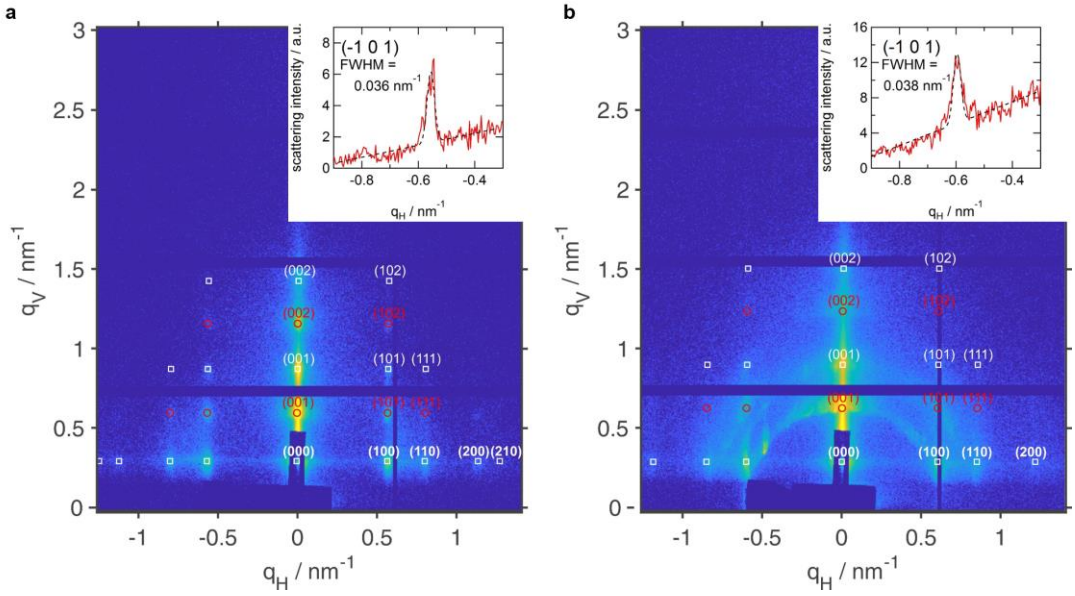

Figure S20. GISAXS image of the superlattices received from zwitterion capped NCs from the same synthesis but different fractions. (a) shows the pattern of NCs from fraction **3s**f2 (7.1 nm) with a tetragonal super unit-cell a =b = 11.0 nm and c = 10.8 nm the super-fluorescence spectrum of which is shown in Figure S23a. (b) shows the pattern of NCs from fraction **3s**f4 (6.7 nm) with a tetragonal super unit-cell a = b = 10.7 nm and c = 10.2 nm the super-fluorescence spectrum of which is shown in Figure S23b. Note that white and red markers correspond to reflected and transmitted scattering contributions of the theoretical lattices, respectively. Insets show peak-fits of the ($\bar{1}$ 0 1) SL reflections to obtain the coherent scattering length (relating to the ordered domain size of the SLs). The obtained

FWHMs of the scattering peaks relate to a mean coherent domain size of $2\pi/FWHM$ = 174 nm and 165 nm for the SLs of fraction **3s**f2 and **3s**f4 respectively.

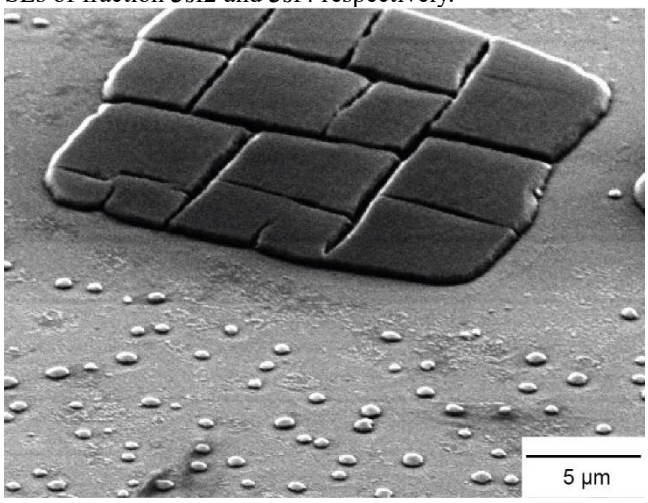

Figure S21. SEM image of a large and several small superlattices acquired under 60° tilt angle and 5 kV acceleration voltage. The sample thickness is ca. 0.5 µm for the large superlattice.

SUPERFLUORESCENCE

For PL spectra in Figure S23 and S24, the sample was mounted in a closed-loop, cold-finger cryostat on an x-y-z-positioning stage and cooled down to a temperature of T = 5 K. The sample was excited with a fiber-coupled excitation laser at an energy of 3.06 eV, in pulsed mode either with 10 or 20 MHz repetition rate (pulse duration 50 ps). The excitation laser output was filtered with a short-pass filter and directed towards the long-working-distance 100× microscope objective (numerical aperture NA = 0.85) by a dichroic beam splitter, resulting in a nearly Gaussian-shaped excitation spot with a $1/e^2$ radius of 1.5 µm. The emission was collected via the same microscope objective. For PL measurements, the collected light was then dispersed by a 300 lines per mm grating inside a 500 mm monochromator and detected by an EMCCD camera. To record time-integrated and time-resolved PL traces at high excitation density (Figure 5 main text), the sample was mounted in a Helium exchange-gas cryostat at 6 K. A frequency-doubled regenerative amplifier seeded with a mode-locked Ti:sapphire laser with a pulse duration of 100–200 fs and a repetition rate of 1 kHz at 3.1 eV photon energy was used as excitation source after passing through short-pass filters (442 nm cut-off wavelength). For both excitation and detection, we used the same focusing lens with 100 mm focal length, resulting in an excitation spot radius of about 60 µm. The recorded PL was long-pass filtered (480 nm cut-off wavelength) and then dispersed by a grating with 150 lines per mm in a 0.3 m-long monochromator and detected with a streak camera with nominal time resolution of 2 ps and instrument response function FWHM of 4 ps. The time-integrated PL spectra were recorded by a 0.5 m-long spectrograph with a grating with 300 lines per mm and a nitrogen-cooled CCD camera.

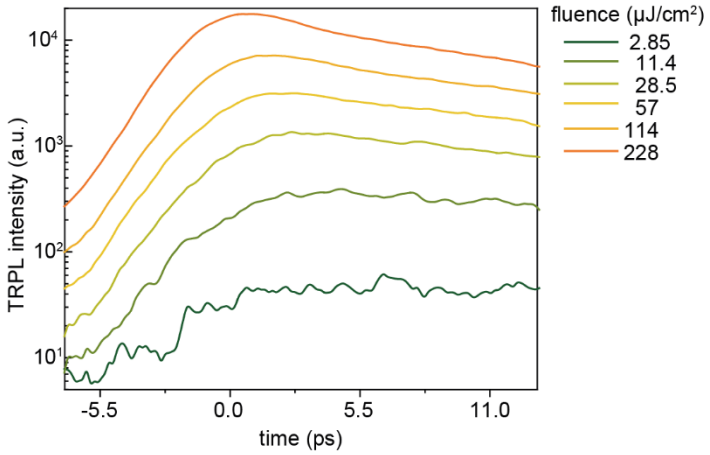

Figure S22. A zoom-in of the spectrally-integrated time-resolved emission intensity traces presented in Figure 5c of the main text. It can be clearly observed that the SF burst peak height increases super-linearly and the SF build-up time shortens at high excitation fluences.

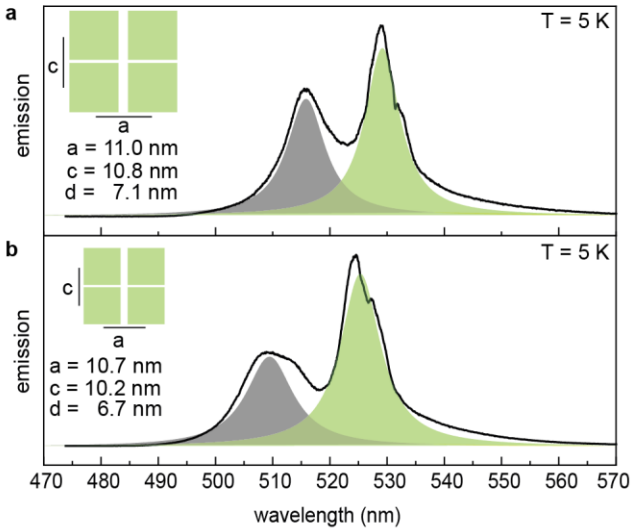

Figure S23. NCs of different fractions of the same NC batch were assembled. (a) **3s**f2 corresponding GI-SAXS data in Figure S20a and (b) **3s**f4 corresponding GI-SAXS data in Figure S20b. The band corresponding to the uncoupled NCs (gray) shifts corresponding to the NC sizes used for the assembly.

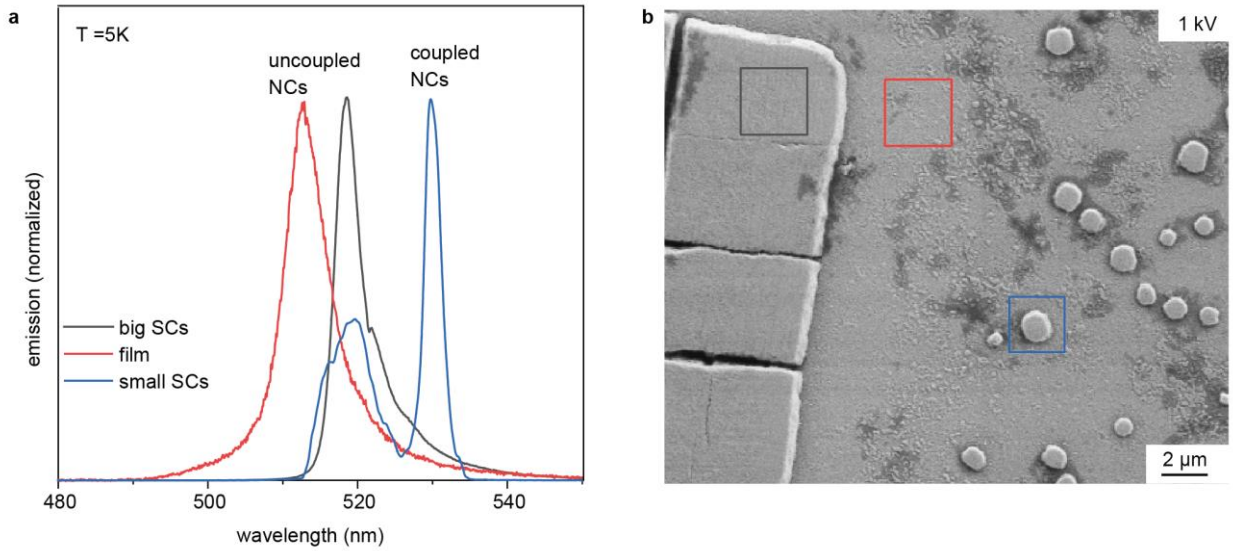

Figure S24. a) Representative PL spectra on different locations on the same sample (assembly of NCs **3s**f2). b) SEM image of that sample. On the same silicon substrate where the supercrystals (SCs) are formed, we find SCs of various sizes. The very big SCs that are readily visible under the optical microscope, do not show super-fluorescence. Their PL emission is red-shifted relative to the continuous NC film that forms from residual NCs in between SCs; the asymmetric PL peak line-shape likely originates from self-absorption.[20] In small SCs, an additionally red-shifted band appeared with the expected features of superfluorescence.

REFERENCES

1. Krieg, F.; Ochsenbein, S. T.; Yakunin, S.; Ten Brinck, S.; Aellen, P.; Suess, A.; Clerc, B.; Guggisberg, D.; Nazarenko, O.; Shynkarenko, Y.; Kumar, S.; Shih, C. J.; Infante, I.; Kovalenko, M. V. Colloidal $CsPbX_3$ (X = Cl, Br, I) nanocrystals 2.0: Zwitterionic capping ligands for improved durability and stability. *ACS Energy Lett.* **2018**, *3* (3), 641-646.
2. Maes, J.; Balcaen, L.; Drijvers, E.; Zhao, Q.; De Roo, J.; Vantomme, A.; Vanhaecke, F.; Geiregat, P.; Hens, Z. Light absorption coefficient of $CsPbBr_3$ perovskite nanocrystals. *J. Phys. Chem. Lett.* **2018**, *9* (11), 3093-3097.
3. Schindelin, J.; Arganda-Carreras, I.; Frise, E.; Kaynig, V.; Longair, M.; Pietzsch, T.; Preibisch, S.; Rueden, C.; Saalfeld, S.; Schmid, B.; Tinevez, J.-Y.; James White, D. J.; Hartenstein, V.; Eliceiri, K.; Tomancak, P. Fiji: an open-source platform for biological-image analysis. *Nat. Methods* **2012**, *9* (7), 676–682.
4. Amenitsch, H.; Bernstorff, S.; Laggner, P. High-performance small- and wide-angle X-ray scattering (SAXS/WAXS) experiments on a multi-functional laboratory goniometer platform with easily exchangeable X-ray modules. *Rev. Sci. Instrum.* **1994**, *66* (2), 1624-1626.
5. Burian, M.; Meisenbichler, C.; Naumenko, D.; Amenitsch, H. SAXSDOG: open software for real-time azimuthal integration of 2D scattering images. *arXiv.org* **2020**, *arXiv:2007.02022*.
6. Glatter, O. Determination of particle-size distribution functions from small-angle scattering data by means of the indirect transformation method. *J. Appl. Cryst.* **1980**, *13*, 7-11.
7. Pedersen, J. S. Analysis of small-angle scattering data from colloids and polymer solutions: modeling and least-squares fitting *Adv. Colloid Interface Sci.* **1997**, *70*, 171-210.
8. Pontoni, D.; Finet, S.; Narayanan, T.; Rennie, A. R. Interactions and kinetic arrest in an adhesive hard-sphere colloidal system. *J. Chem. Phys.* **2003**, *119* (12), 6157-6165.
9. Becker, M. A.; Vaxenburg, R.; Nedelcu, G.; Sercel, P. C.; Shabaev, A.; Mehl, M. J.; Michopoulos, J. G.; Lambrakos, S. G.; Bernstein, N.; Lyons, J. L.; Stoferle, T.; Mahrt, R. F.; Kovalenko, M. V.; Norris, D. J.; Raino, G.; Efros, A. L. Bright triplet excitons in caesium lead halide perovskites. *Nature* **2018**, *553* (7687), 189-193.
10. Brus, L. E. Electron–electron and electron-hole interactions in small semiconductor crystallites: The size dependence of the lowest excited electronic state. *J. Chem. Phys.* **1984**, *80* (9), 4403-4409.
11. Sercel, P. C.; Lyons, J. L.; Wickramaratne, D.; Vaxenburg, R.; Bernstein, N.; Efros, A. L. Exciton fine structure in perovskite nanocrystals. *Nano Lett.* **2019**, *19* (6), 4068-4077.
12. Sercel, P. C.; Lyons, J. L.; Bernstein, N.; Efros, A. L. Quasicubic model for metal halide perovskite nanocrystals. *J. Chem. Phys.* **2019**, *151* (23), 234106.
13. Brennan, M. C.; Herr, J. E.; Nguyen-Beck, T. S.; Zinna, J.; Draguta, S.; Rouvimov, S.; Parkhill, J.; Kuno, M. origin of the size-dependent stokes shift in $CsPbBr_3$ perovskite nanocrystals. *J. Am. Chem. Soc.* **2017**, *139* (35), 12201-12208.
14. Zhao, Q.; Hazarika, A.; Schelhas, L. T.; Liu, J.; Gaulding, E. A.; Li, G.; Zhang, M.; Toney, M. F.; Sercel, P. C.; Luther, J. M. Size-dependent lattice structure and confinement properties in $CsPbI_3$ perovskite nanocrystals: Negative surface energy for stabilization. *ACS Energy Lett.* **2019**, *5* (1), 238-247.
15. Utzat, H.; Shulenberger, K. E.; Achorn, O. B.; Nasilowski, M.; Sinclair, T. S.; Bawendi, M. G. Probing linewidths and biexciton quantum yields of single cesium lead halide nanocrystals in solution. *Nano Lett.* **2017**, *17* (11), 6838-6846.
16. Yang, Z.; Surrente, A.; Galkowski, K.; Miyata, A.; Portugall, O.; Sutton, R. J.; Haghighirad, A. A.; Snaith, H. J.; Maude, D. K.; Plochocka, P.; Nicholas, R. J. Impact of the halide cage on the electronic properties of fully inorganic cesium lead halide perovskites. *ACS Energy Lett.* **2017**, *2* (7), 1621-1627.
17. Rahsba, E. I.; Gurgenishvili, G. E. Edge absorption theory in semiconductors. *Sov. Phys. Solid State* **1962**, *4*, 759-760.
18. Ilavsky, J. Nika: software for two dimensional data reduction. *J. Apll. Cryst.* **2012**, *45*, 324-328.
19. Jiang, Z. GIXSGUI: a MATLAB toolbox for grazing-incidence X-ray scattering data visualization and reduction, and indexing of buried three-dimensional periodic nanostructured films *J. Appl. Cryst.* **2015**, *48*, 917-926.
20. Baranov, D.; Toso, S.; Imran, M.; Manna, L. Investigation into the photoluminescence red shift in cesium lead bromide nanocrystal superlattices. *J. Phys. Chem. Lett.* **2019**, *10* (3), 655-660.